Flow Control over a Rotorcraft Blade Modeled by a Boeing VR-7 Airfoil

Thesis

For the Fulfillment of the Honors Research Requirement

By

Achal Singhal

Undergraduate Program in Mechanical Engineering

The Ohio State University

2015

Examination Committee:

Dr. Mo Samimy, Advisor

Dr. Datta Gaitonde

ABSTRACT

This study is motived by the dynamic stall of rotorcraft blades. Dynamic stall is an attribute of airfoils that undergo a rapid change in their angle of attack and thus is common in rotorcraft blades. It is desired to control dynamic stall as it causes unsteady lift in a rotor blade, inducing performance penalty as well as mechanical fatigue of this component. Current experimental techniques, such as momentum addition have been shown to be effective, but are undesirable due to structural considerations and Reynolds number limitations. Current developments and research with surface mounted nanosecond pulse driven dielectric barrier discharge (NS-DBD) plasma actuators have been shown to increase the critical angle of attack by controlling flow instabilities over the airfoil for fixed wing aircraft to eliminate the flow separation from the airfoil at high angles of attack. In the study, a Boeing VR-7 airfoil, a common rotorcraft blade profile, is placed in static stall with a NS-DBD actuator in a wind tunnel, at a post stall angle of attack. The lift and drag characteristics were measured and the wake flow field was visualized using laser diagnostic techniques. Experimentation indicates the efficacy of the actuators to increase lift with minimal increases in drag at high excitation Strouhal numbers. At the optimal excitation Strouhal number, the energy addition of actuations is 0.09% of the freestream energy. The increase in lift is 25%, whereas the drag plenty is 3%. Although complete reattachment of the flow is not observed, it is observed that each pulse of the actuator generates a vortex that convects downstream, entraining high speed flow into the separated region and thus at higher excitation Strouhal numbers, there is an increase in the coefficient of lift.

DEDICATION

I would like to dedicate this paper to all those who have invested so much in helping me succeed – thank you!

ACKNOWLEDGEMENTS

I am grateful to Dr. Samimy for all that he has done in making this opportunity a wonderful learning experience.

I would also like to thank all of my laboratory collegues, especially Chris Clifford and Cameron DuBois for their mentorship throughout the years.

I would like to thank the Ohio Space Grant Consortium and the Ohio State University with providing me the means to engage in undergraduate research. I

TABLE OF CONTENTS

TABLE OF FIGURES

I. Introduction

Flow control is an important aspect in creating energy efficient vehicles, by increasing the amount of lift produced or reducing the drag produced by an airfoil. An increased lift allows for an aircraft to have a larger payload, or a shorter takeoff distance. A lesser drag, leads to a more efficient system of travel. Thus, flow control is an attractive option to reduce operating costs of a vehicle by decreasing the amount of fuel used in a given flight. Many flow control options can be readily incorporated into existing systems, allowing for a shorter implementation time and a more cost effective approach than the design of a new vehicle.

Flow control can be either passive or active. Passive flow control techniques can be a simple and elegant solution to many flow control applications. Passive flow control techniques involve geometric modifications to the object. One example is a vortex generator. These devices are placed on wings to generate tip vortices that entrain high speed flow to the boundary layer and delays flow separation. This allows for a greater generation of lift. However they suffer from a limited operating band. Active control techniques require the use of a mechanical or electrical device with an external power source. Perhaps not as simple as their passive counterparts, these techniques have the capability of adapting to various flow regimes and thus are more flexible in their application.

One such application is rotorcraft, such as helicopters. Rotorcraft achieve flight via the use of wings attached to a rotating shaft. The rotation of these blades increases the local flow velocity of the blade, thus allowing them to produce lift.

The local flow velocity seen by a point on the blade is the sum of both the rotational velocity as well as the mean velocity of the vehicle. Thus, any movement of the vehicle will

lead to a discrepancy in the symmetry of the velocity profile along the rotor blade. This gives rise to two primary regimes of the rotor blade, an advancing and retreating side. The advancing blade sees a higher velocity than the retreating blade, as shown in Fig. 1. A third regime of reverse flow also exists on the retreating side. This regime is characterized by a negative velocity, or that air flow around this portion of the blade travels backward with respects to the airfoil geometry. For helicopters, this region is small due to the high rotational velocity of the blade, but can be significant in slowed-rotor designs. Slowed-rotor compound vehicles consist of a large rotor to generate lift at low flight speeds as well as secondary propulsion systems and fixed wings to generate lift at higher velocities.

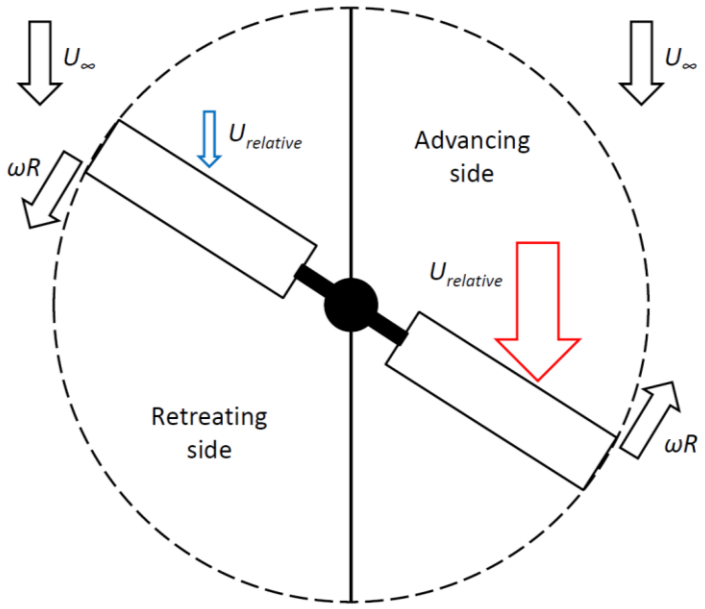

Fig. 1. Illustration of Local Velocity on Advancing and Retreating Blade Sides [2]

Given that the lift force is proportional to the velocity squared, the asymmetry of velocity gives rise to the phenomena known as asymmetry of lift. Without any correction for the lift, the advancing side of the rotorcraft would provide more lift force than the retreating side

and the rotorcraft would roll—an undesirable flight condition. To ensure stable flight variable pitch blades are used. By changing the angle of attack with regards to the blade position, the lift force produced can be controlled. As such, the pitch of the blade is the lowest in the advancing side and the highest in the retreating side.

The constant change in pitch of the airfoil is undesirable as it introduces mechanical complexity and causes another flow phenomenon known as dynamic stall. Dynamic stall is caused by a rapid change in angle of attack. This rapid change causes the formation of a vortex, which entrains high velocity flow to the surface of the blade. However, after the vortex is shed, the airfoil is in stall, and the blade loses its ability to generate lift.

Active control techniques primarily consist of momentum injection generally by blowing or exciting shear layer instabilities via pulsed blowing. Momentum injection has been shown to be successful in the separation of the dynamic stall vortex [3]. Pulsed blowing has produced successful results as well, and functions by exciting flow instabilities [3, 4]. In this technique, there is often an optimal frequency and location (which tends to be near the point of flow separation) [4]. However, even in pulsed blowing, as the freestream velocity increases, so does the required momentum injected for these active control techniques to be successful [5]. In addition, the addition of slots (for blowing) in rotor blades may compromise the structural integrity and thus are not as desirable [3].

Nanosecond pulse driven dielectric barrier discharge (NS-DBD) plasma actuators are surface mounted actuators and thus may provide a desired solution. NS-DBD plasma actuators have been given much attention for their high control authority at large Reynolds numbers [6]. These actuators consist of two copper electrodes separated by a dielectric barrier. When a large voltage is applied, this forces an electrical breakdown of the nearby

air and via Joule heating causes a rapid expansion of the air [6]. When pulsated, this rapid expansion manifests itself as a pressure wave and can be used to excite flow instabilities [6]. As such, they function similarly to pulsed blowing techniques and may be a viable alternative to jets. As a precursor to dynamic stall experiments, these actuators will be mounted to the Boeing VR-7 airfoil in static configuration to determine optimal parameters, such as frequency, of the actuators.

II. Background Information

Helicopters and other rotorcraft represent a large number of vehicles used in fire, rescue, and ambulance services as well as in military applications. These vehicles have the ability to perform vertical take-off and hover capabilities that exceed their fixed wing counter parts. However, dynamic stall constrains the potential of these vehicles, by imparting large impulsive loads on the rotor blades. These loads can introduce vibrations that fatigue the mechanical systems and are detrimental to the health of the crew [3].

A. Dynamic Stall

The flow velocity over the rotor blade is not constant, as shown in Fig. 2 [7]. The local flow velocity is a linear combination of both the flight velocity and the rotational speed of the rotorcraft. The retreating side of the rotor blade sees a lower flow velocity in general as compared to the advancing blade. Therefore, the net lift produced will be offset form the center of the craft and leads to lift asymmetry. Unaccounted for, this prevents stable flight. As such, the angle of attack is lowered during the advancing portion of the blade, and increased during the retreating phase.

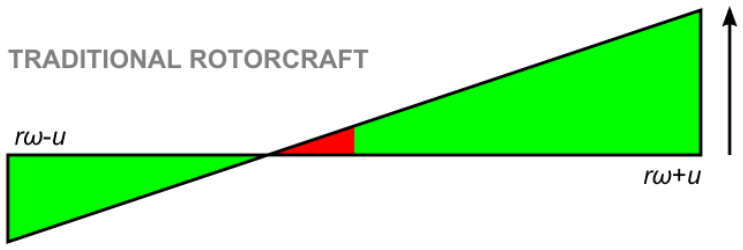

Fig. 2. Local Velocity over a Rotor Blade, where Red Areas Represent Reversed Flow [7]

This change in angle of attack leads to dynamic stall. As the angle of attack increases and exceeds the steady stall angle, a leading-edge bubble forms. This bubble will grow into

the dynamic stall vortex, which will momentarily increase the lift produced. This is followed by a fully separated flow and significantly decreased lift. As the angle of attack decreases, the flow will recover to its initial state. Dynamic stall differs from static stall, in that the flow remains unsteady, and thus the lift will by cyclic with respects to the motion of the airfoil, which introduces unsteady loads on the rotor. Furthermore, the formation of dynamic stall vortex as well as the momentarily increased lift are also unique to dynamic stall. Smoke flow visualization of dynamic stall of a Boeing Vertol VR-7 airfoil that pitches from 5°to 25°is shown in Fig. 3 [3].

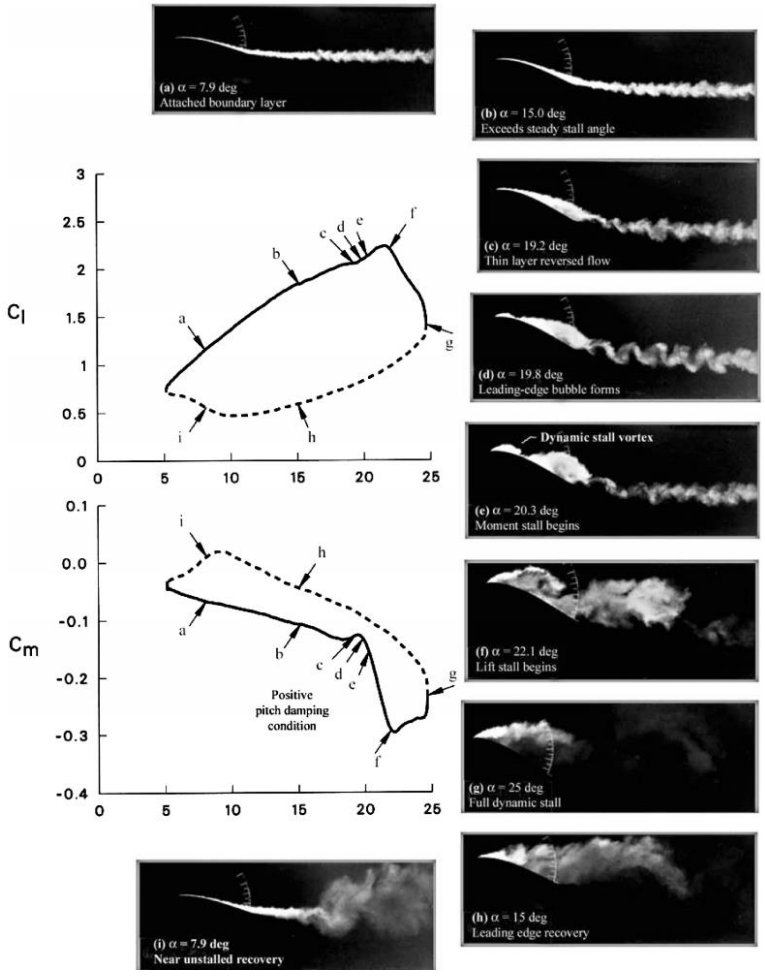

Fig. 3. Smoke Flow Visualization of Dynamic Stall [3]

B. Flow Control

Currently, both passive and active flow control techniques are being explored for maintaining lift during dynamic stall. Passive techniques rely on geometric modifications to the airfoil. These modifications are effective at design conditions, but readily lose efficacy at off-design operating points. For example, Martin et al. have successfully applied counter rotating vane type vortex generators in light stall and low velocity cases [8]. However, at deep stall, or at higher velocities; these vortex generators were insufficient [8].

Active flow control techniques include blowing and plasma actuation. Unlike passive techniques, active flow control requires the use of actuators powered by an external source. These systems tend to function by either momentum injection generally by blowing, or by exciting shear layer instabilities via pulsed actuation. Pulsed actuation is an effective means of flow control [1] and requires less energy input then continuous actuation. Despite the smaller energy consumption, pulsed actuation can be as or more effective than steady blowing [9].

Momentum injection via blowing has been shown to be effective in the suppression of the dynamic stall vortex [3]. In doing so, the drag forces are substantially decreased, and the lift and drag loads on the rotor blade remain steady. However, a major drawback of momentum injection is that momentum injections becomes limited at high velocities without the use of additional power. Furthermore, the addition of slots in a rotor blade is a complex and expensive endeavor and thus is undesirable.

Plasma actuators are a newer class of active control devices. These actuators consist of two electrodes separated by a dielectric barrier, as shown in Fig. 4. Depending on the driving voltage source, the behavior of these actuators can change dramatically. An alternating

current driven dielectric barrier discharge (AC-DBD) plasma actuator utilizes its high positive charge to ionize the quiescent air. This plasma is then attracted to the ground electrode and thus accelerates the surrounding air. As such, AC-DBD plasma actuators are often used to generate blowing. These actuators are a viable alternative to blowing—the actuators produce a similar net effect as jets, but with less mechanical complexity. These types of actuators are typically operated at a fixed frequency based on the electrical properties of the circuit, but may be modulated to lower frequencies for the purpose of exciting flow instabilities. However, similar to blowing techniques, these actuators are limited at high flow speeds.

An alternative driving signal is a high voltage, short duration pulse. Known as nanosecond pulse driven dielectric barrier discharge (NS-DBD) plasma actuators, these actuators use Joule heating to create compression waves that can be used to excite flow instabilities. These types of actuators have very high bandwidth, low energy consumption (0.054 milliwatts per centimeter per pulse), and have been proven in high velocity flows [10]. Thus these actuators function similar to pulsed blowing, but do not have the same high-speed limitations of momentum injection.

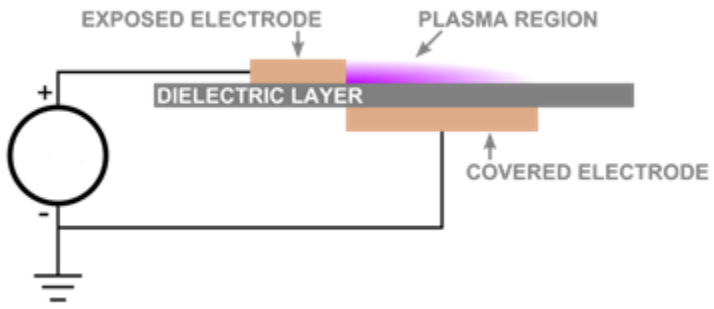

Fig. 4. Plasma Actuator Construction [7]

C. Nanosecond Dielectric Barrier Discharge Plasma Actuators

NS-DBD plasma actuators consist of two electrodes separated by a dielectric barrier. When a high voltage (5-20 kilovolts) is applied to the exposed electrode for a short duration (tens of nanoseconds) a cylindrical compression wave is generated, as shown in Fig. 5 [11]. In the figure, there is a bright spot at the location of the plasma (near $y = 1.25$ millimeters).

The cylindrical compression is actually the sum of a series of spherical waves due the localized heating of the fluid [12]. As such, the thermal mechanism is not as sensitive to flow velocities, compared to momentum-based actuation.

Fig. 5. Phase – Averaged Schlieren of Compression Wave [13]

NS-DBD plasma actuators have been proven efficacious in flow control applications in both airfoil and bluff body flow. Rethmel et al. showed that NS-DBD plasma actuators behave as active boundary layer trips at low Reynolds numbers [14]. However at high Reynolds numbers and post stall angle of attacks, the NS-DBD plasma actuator can trigger

the growth of flow instabilities to generate coherent structures at certain frequencies [14]. These structures increase the coefficient of lift by entraining freestream flow and reattach the separated flow. Thus they can allow the airfoil to operate at high angle of attacks. Little et al. obtained similar results—namely that at certain frequencies, NS-DBD plasma actuators can re-attach flow at high velocity and at post-stall angle of attacks [6].

More recent developments with NS-DBD plasma actuators indicate its efficacy in bluff body flows [15, 10]. Mounted on the aerodynamic leading edge of an airfoil where the aerodynamic leading edge was coincident with the geometric trailing edge, the NS-DBD plasma actuator demonstrated significant control authority [15].

As a next step, and the primary focus of this thesis, the NS-DBD plasma actuator will be mounted to the Boeing Vertol VR-7 airfoil in a static configuration to determine the efficacy of the actuators on a more representative geometry.

As such, in the retreating and advancing portions of the rotor blade, where the flow characteristics can vary immensely, the same actuators can be used to with different frequencies applied. This characteristic makes these actuators well suited in a rotorcraft.

III. METHODOLOGY

All experiments were performed at the Gas Dynamics and Turbulence Laboratory at the Ohio State University.

A. Facility

Experimentation was conducted in a closed, recirculating wind tunnel that is capable of producing flow velocities from 3 – 95 meters per second. The flow is generated by an axial fan powered by a variable AC induction motor. Turning cascades are used to minimize losses within the tunnel and the flow is conditioned using a hexagonal-cell aluminum honeycomb prior to entering the test section. As a result, the freestream turbulence varies between 0% and 1.25%. A heat exchanger is used to steady the freestream temperature.

The test section measures 61 x 61 x 122 centimeters with 25.4 millimeter thick acrylic walls. Each side wall contains a port with a diameter of 30.5 centimeters and is centered with respects to the side wall geometry. Between these ports, the airfoil is mounted. As such, their rotation allows for testing a given airfoil at any angle of attack.

In the ceiling of the wind tunnel, there is a slot, which allows for the deployment of various sensors into the flow field. The slot is covered by a high-density nylon brush. A two-dimensional traverse system is mounted to the ceiling of the wind tunnel and allows the precise placement of sensors using lead screws.

The total and static pressure conditions of the wind tunnel are measured using two piezometer rings, consisting of four pressure taps each, at either end of the converging section. Pressure transducers manufactured by Omega Engineering, Inc. (PX655-25DI and PX655-5DI) are used to take measurements of the tunnel conditions. A thermocouple is also used to monitor the tunnel temperature. From these parameters, the Reynolds number (Re)

is determined by Eq. 1, where u_∞ is the freestream velocity, c is the chord length and ν is the kinematic velocity. Throughout this thesis, the Reynolds number was kept at 500,000.

$$Re = \frac{u_\infty c}{\nu} \quad (1)$$

B. Airfoil

A Boeing Vertol VR-7 airfoil manufactured from a non-conductive composite was utilized. The airfoil has a chord length, c (or L), of 20.3 centimeters and spans the entire width of the wind tunnel. To ensure that the actuator is flush mounted, a shallow recess of 0.76 millimeters is placed from a position of $x/c = 0.1$ chord on the pressure side to a position of $x/c = 0.35$ chord on the suction side. This is illustrated in Fig. 6.

For the purposes of this study, the absolute coordinate system is fixed to the leading edge of the airfoil. The direction parallel to the freestream velocity and downstream of the leading edge is considered to be positive x axis. The y axis is orthogonal to the x axis. Both axes are normalized by the length of the chord of the airfoil. The angle of attack, defined to be the angle between the chord line and the freestream velocity, was kept at post stall angle of 17° during experimentation.

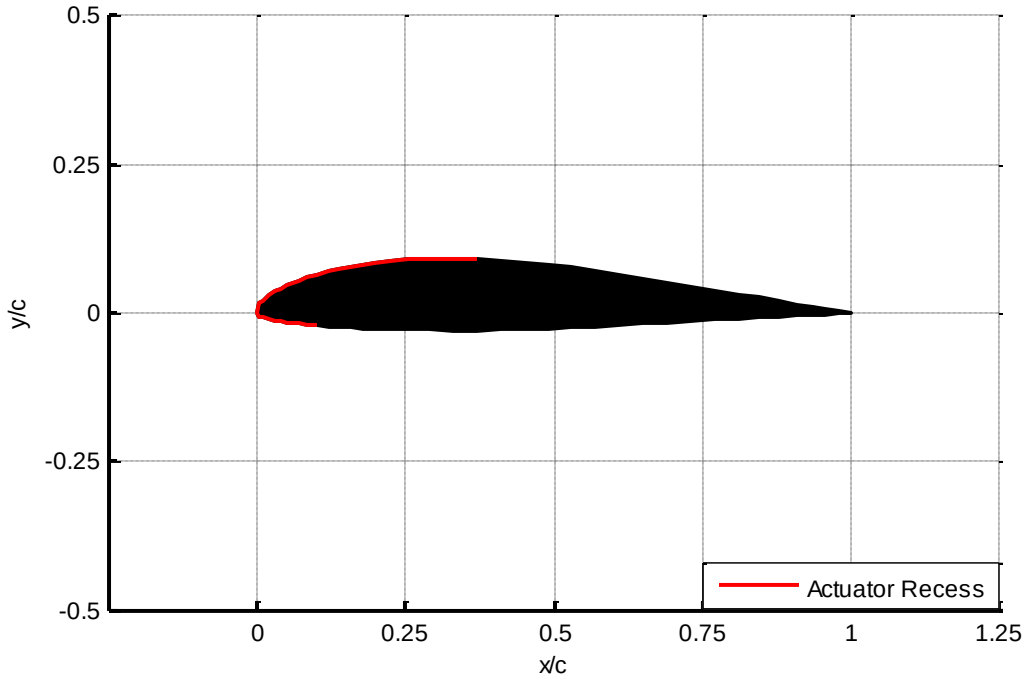

Fig. 6. Actuator Recess and Coordinate System

The airfoil is hollow to allow for the placement of instrumentation, but does contain chord-wise ribs for structural rigidity. Two span-wise spars protrude from the main body of the airfoil to allow the mounting of the airfoil to the wind tunnel.

C. Oil Flow Visualization

Oil flow visualization provides a qualitative understanding of the flow along the surface of the airfoil and as well as a means of measuring flow features (such as separation location). During experimentation, titanium white oil-based paint is mixed with SAE 85W-140 gear oil with a ratio of 10 parts of paint to 1 part of oil. It was primarily used to determine the flow separation location at the leading edge.

The paint and gear oil mixture is applied to the airfoil using span-wise strokes. The wind tunnel is then sped to the desired operating velocity and allowed to run until the flow features

in the paint are clearly defined, as shown in Fig. 7. The light green indicates the point of separation.

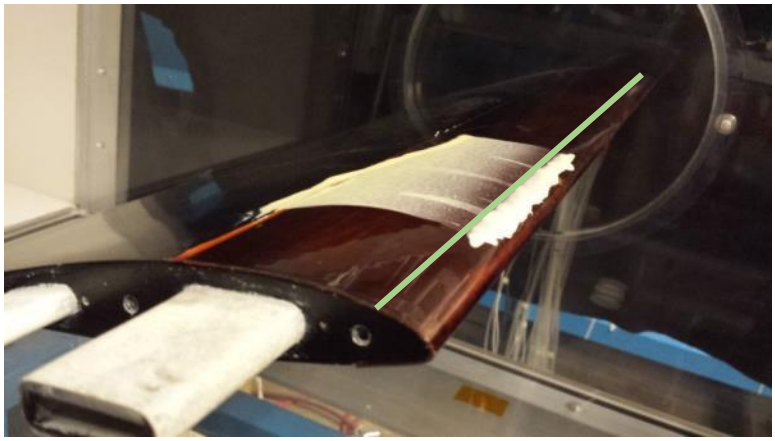

Fig. 7. Sample Oil Flow Visualization with Clearly Defined Separation

D. Static Pressure Measurements

The airfoil has 33 static pressure taps distributed along the surface of the airfoil. The density of the pressure taps is greater at the leading edge, which is indicated in Fig. 8. Any pressure taps covered by an electrode of the plasma actuators were excluded in any data analysis. However, pressure taps covered only by Kapton tape were still used. In these cases, the overlaying tap was pierced through such that the pressure taps could be used.

The pressure signals are recorded using three Scanivalve digital pressure sensor arrays (DSA-3217) at a frequency of 1 Hz and a total sample size of 100 samples. For excited cases, the sample size was reduced to 50 samples and two sets of data were taken. These measurements are then averaged and the coefficient of pressure, C_p, is computed using Eq. 2. In this equation, P is the local static pressure, P_∞ is the freestream pressure, and Q_∞ is the freestream dynamic pressure.

$$C_p = \frac{P - P_\infty}{Q_\infty} \quad (2)$$

From the coefficient of pressure, the coefficient of lift, C_L, and the coefficient of pressure drag, C_D, can be computed by integrating the coefficient of pressure, C_p, over the surface of the airfoil. The equations are shown in Eq. 3 and Eq. 4, where θ is the angle between the normal of the surface of the airfoil and the freestream velocity. The integration is conducted over the surface of the airfoil, where -1 is located on the trailing edge along the pressure side, 0 is located on the leading edge, and 1 is located on the trailing edge along the suction side.

$$C_L = -\int_{-1}^{1} C_p \, sin(\theta) \, ds \tag{3}$$

$$C_D = -\int_{-1}^{1} C_p \, cos(\theta) \, ds \tag{4}$$

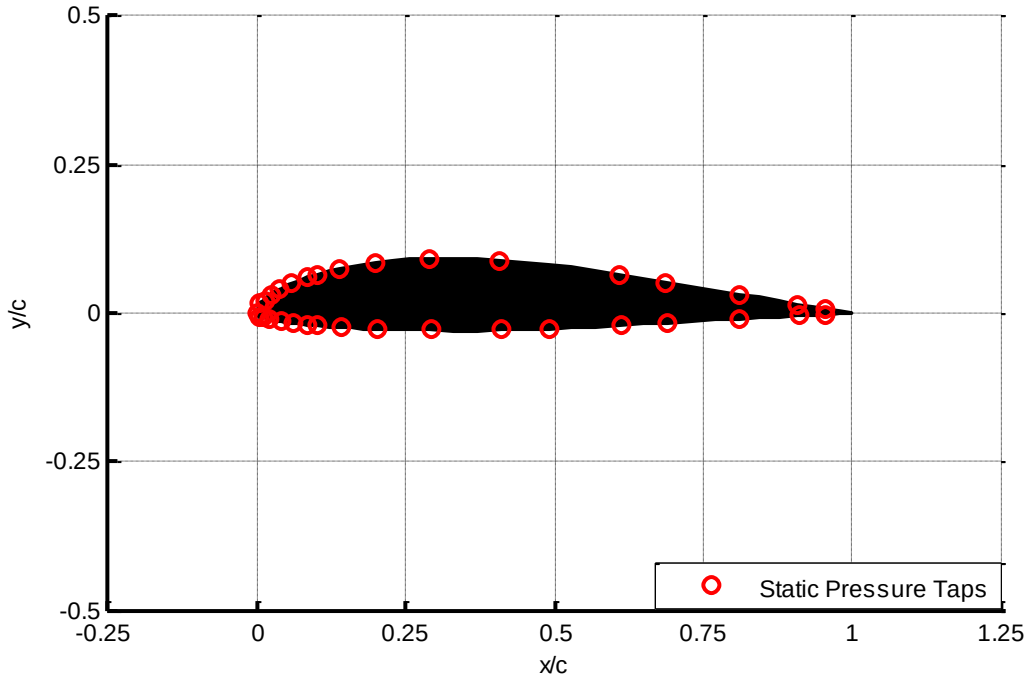

Fig. 8. Static Pressure Taps

E. Fluctuating Pressure Measurements

Fluctuating pressure data in the flow field is taken using a Bruel and Kjaer model 4939 microphone with a Nexus 2690 signal conditioner and amplifier. The microphone is calibrated using a Bruel and Kjaer 4231 acoustical calibrator (generating a 1 kilohertz and 94 decibel signal). The microphone is mounted to the traverse system described previously and inserted into the wind tunnel using the slot in the ceiling.

The microphone is placed outside of the shear layer to capture pressure signals from the flow field as determined from particle image velocimetry data. The data location is a function of both the angle of attack and the Reynolds number. During experimentation, these experimental parameters were kept at 17° and 500,000, respectively. In this flow regime, the microphone was located at $x/c = 1.75$ and $y/c = 0.4375$ (Fig. 9). The position of the microphone was determined such that the spectra was dominated by pressure signals due to vortex shedding among other wake interactions and such that a shedding peak was observed.

It is important to note that the microphone is placed far downstream and thus will only capture large structures in the wake. As such, these results should be interpreted with caution.

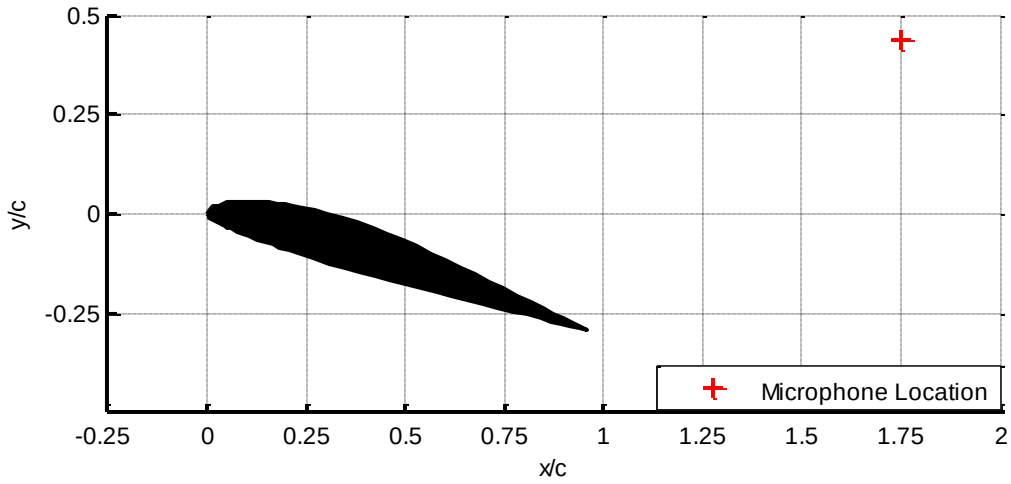

Fig. 9. Microphone Location

F. Particle Image Velocimetry

Two-component particle image velocimetry (PIV) is used to obtain both a qualitative and quantitative understanding of the flow physics. A LaVision 1108926 particle seeder is used to place sub-micron di-ethyl-hexyl-sebacat (DEHS) seed particles upstream of the wind tunnel test section. Sheet forming optics, comprised of various spherical and cylindrical lenses, are used to create a thin laser sheet from a beam produced by the Spectra Physics PIV-400 Nd:YAG laser. The time between pulses is such that a particle in the freestream displaces by 5 pixels.

Side by side LaVision 14-bit 2048×2048 pixel Imager Pro-X CCD cameras with Nikon Nikkor 50 mm F/1.2 lens are used to obtain a wide view of flow over the airfoil and wake. Cross-correlations of window sizes of 64 pixels and 32 pixels are used, with multi-

pass processing of 50% and 75% overlap, to compute the preliminary vector fields. The vector fields are then post-processed by removing spurious vectors and applying a 3×3 Gaussian smoothing filter.

Two sets of 300 images acquired at 5 hertz are taken for each data set. These two sets are then averaged together to produce ensemble-averaged images. From the ensemble-averaged particle image velocimetry, the separation area, A_{sep}, was defined as the area between the airfoil and the zero velocity iso-contour.

Particle image velocimetry images are also acquired by phase locking to the actuator pulses in increments of $90°$. Two sets of 300 images were acquired at the excitation frequency and then averaged together.

G. Plasma Actuators

NS-DBD plasma actuators consist of two copper electrodes separated by a dielectric barrier (Fig. 10). In this application, the exposed electrode had a width of 6.35 millimeters and the covered electrode had a width of 12.7 millimeters. Both electrodes were 0.09 millimeters thick. These actuators are separated by three layers of Kapton tape, each with a thickness of 0.09 millimeters. Thus dielectric thickness was 0.27 millimeters. The total thickness of the entire actuator is 0.45 millimeters.

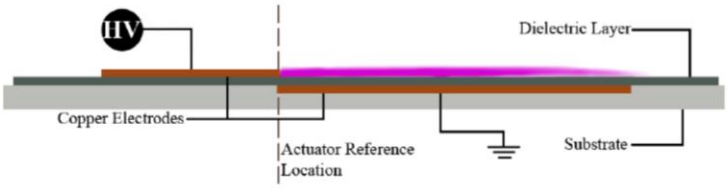

Fig. 10. NS-DBD Plasma Actuator Construction

As indicated in Fig. 11, there is a single actuator installed on the suction side of the airfoil. The location of the actuator was upstream of the separation location as determined by oil flow visualization. Previous experimentation and literature review ([6], [14]) indicates the optimality in placing the actuator in this manner [5,9]. Again, this location is sensitive to both the Reynolds number and angle of attack. For the experimental parameters given above, the separation location was determined to be at $x/c = 0.039$ on the suction side by oil flow visualization.

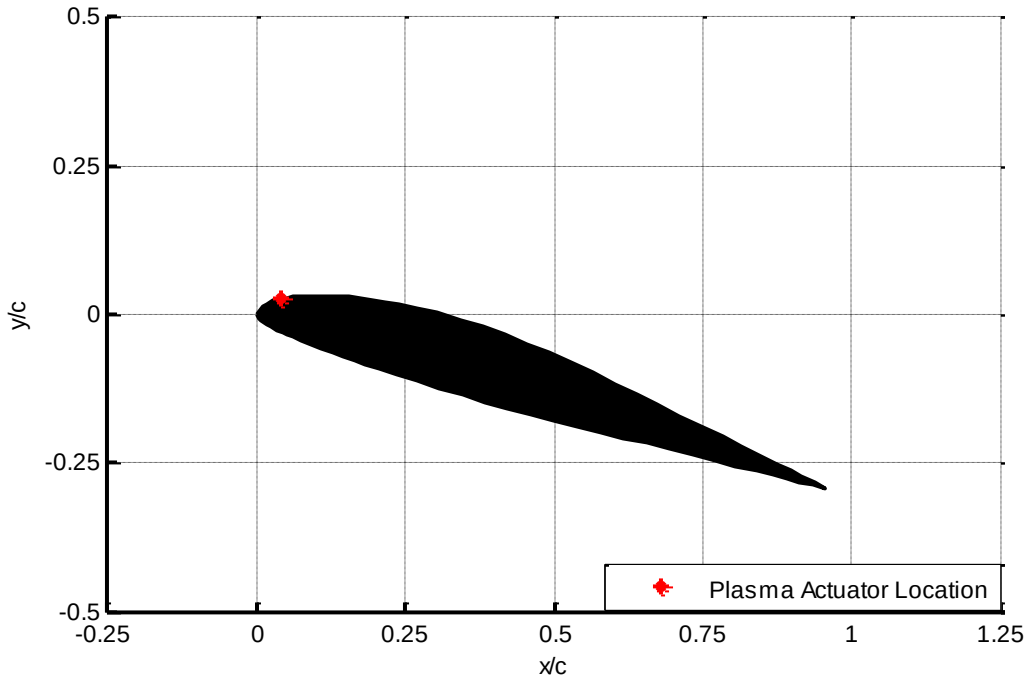

Fig. 11. NS-DBD Plasma Actuator Location

For excited cases, the excitation Strouhal number, St_e, was used to normalize the forcing frequency. In Eq. 5, f is the excitation frequency, c is the chord length, and u_∞ is the freestream velocity.

$$St_e = \frac{fc}{u_\infty} \tag{5}$$

The actuators are powered by a custom high voltage magnetic compression type pulse power supply. This power supply is not unique to this study and a more detailed analysis is provided by Little et al. [13]. The pulses generated by the power supply have a full-width at half-max of approximately 90 nanoseconds, and its magnitude is dependent on the DC voltage and actuator loading. For excited cases in this study, the DC voltage was set to 450 volts and the energy per pulse was 3 millijoules per pulse. Typical voltage, current, power, and energy curves for a 56 centimeter actuator are provided in Fig. 11 and Fig. 12.

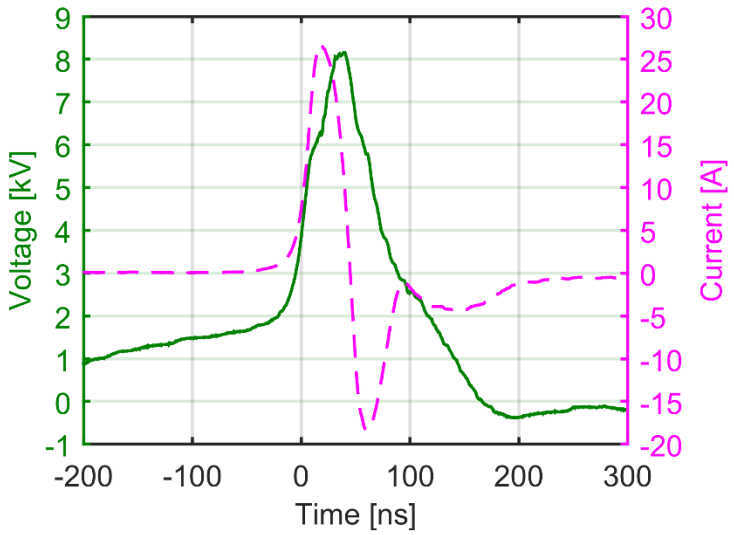

Fig. 12. Power Supply Voltage and Current Traces

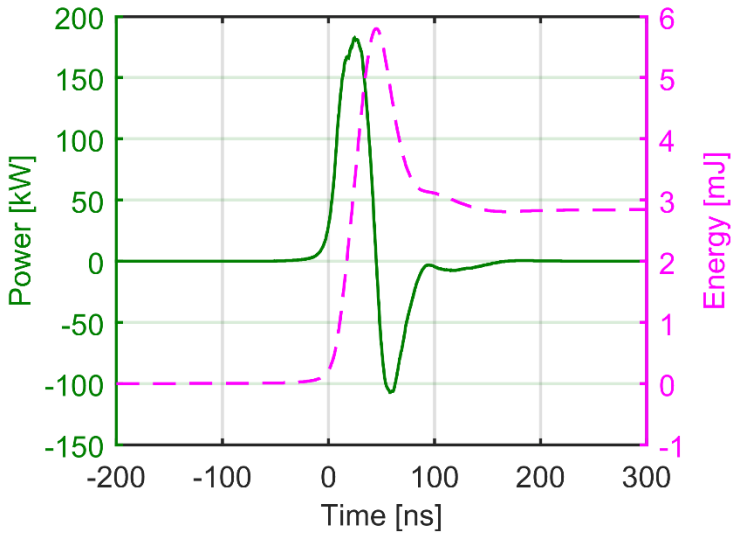

Fig. 13. Power Supply Power and Energy Traces

Baseline Results

Prior to excitation, the airfoil was characterized and then baseline (non-excited) data was acquired at a Reynolds number of 500,000 and an angle of attack of 17°, which is a deep stall condition.

A. Airfoil Characterization – Baseline Surface Pressure Data

Surface pressure data was obtained from the surface pressure taps located about the airfoil to characterize the airfoil in various flow regimes. As a precursor to any flow field data collection, lift and drag curves were compared to XLFR5, a viscid numerical flow solver to ensure the fidelity of the airfoil.

The coefficient of static pressure distribution over the airfoil for varying Reynolds numbers and angle of attacks are shown in this section (Fig. 14, Fig. 15, and Fig. 16). Only a subset of the full data set is shown in these figures. In the analysis of these figures, a coefficient of pressure of 1 indicates a stagnation point and an increase in the coefficient of pressure with respects to x/c ($\frac{dC_p}{d(x/c)} > 0$) indicates a favorable pressure gradient. This helps the flow remain attached to the airfoil. A constant coefficient of pressure ($\frac{dC_p}{d(x/c)} = 0$), indicates that the flow is detached.

Fig. 14 shows sample coefficient of pressure distributions for select angle of attacks at a Reynolds number of 200,000. At a near zero angle of attack, the coefficient of pressure curve near the leading edge for the top and bottom surfaces is separated before collapsing onto a single curve and furthermore the coefficient of pressure is small. The majority of the lift generated is by the main body of the airfoil as opposed to the leading edge. This is in contrast to the 12° angle of attack, where the majority of the lift is generated by the leading edge. At 17°, the flow becomes fully separated.

These trends are also seen at a Reynolds number of 500,000 and 1,000,000 (Fig. 15 and Fig. 16, respectively). However at a Reynolds number of 1,000,000 and an angle of attack of 17°, the flow separation point moves downstream of the leading edge to $x/c = 0.15$.

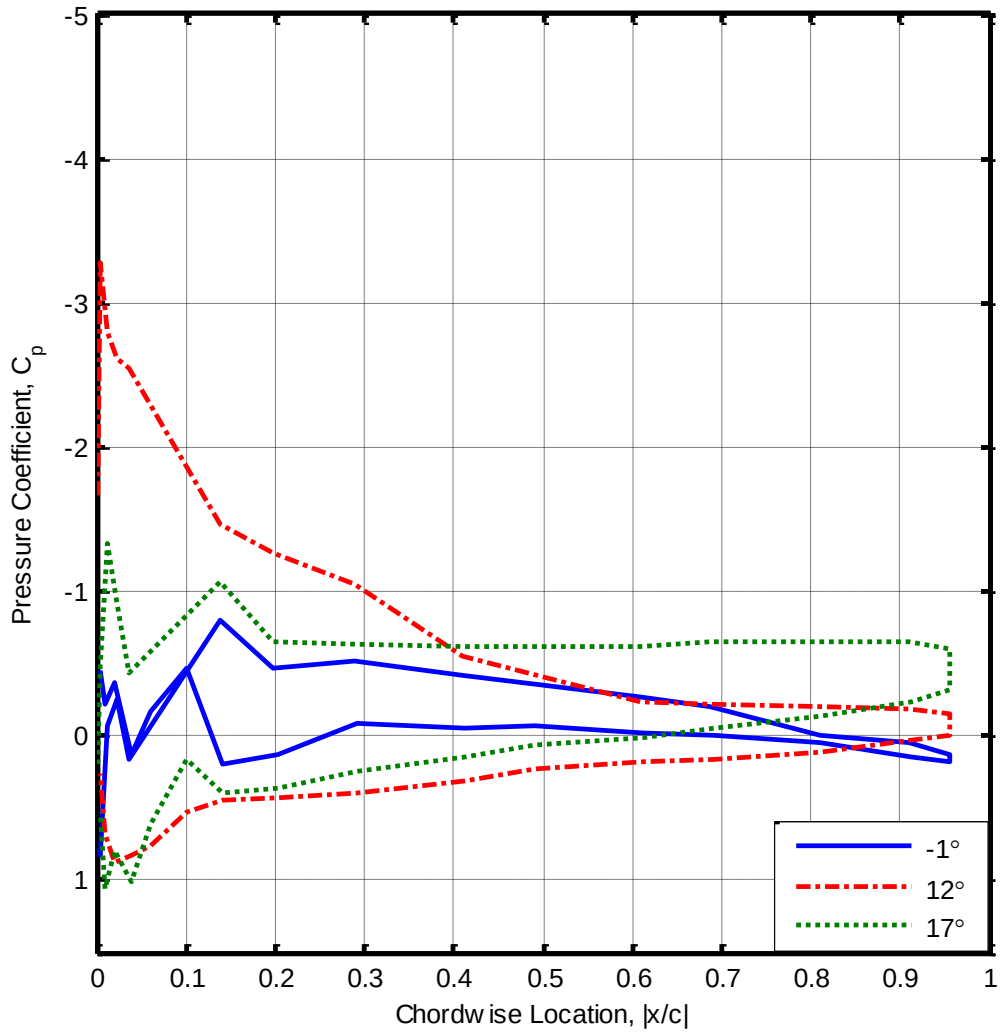

Fig. 14. C_p Distribution at a Reynolds Number of 200,000

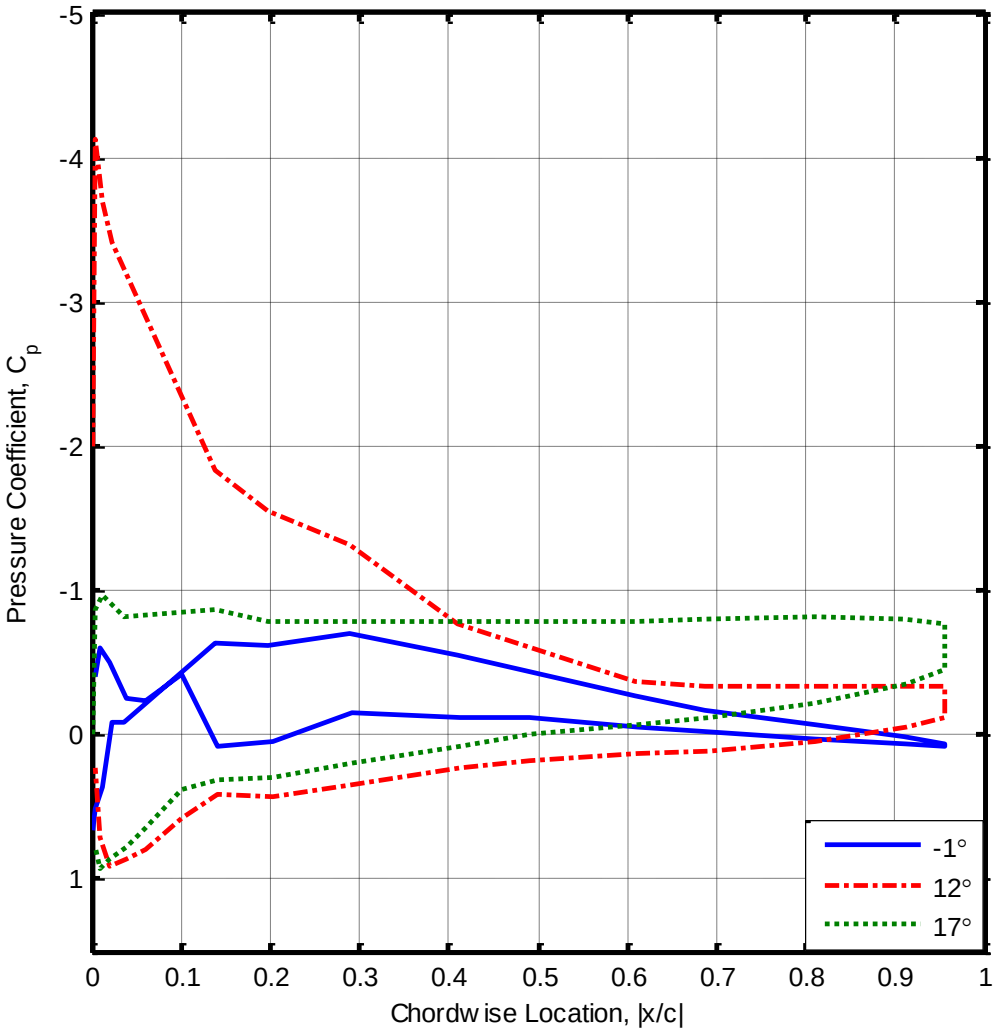

Fig. 15. C_p Distribution at a Reynolds Number of 500,000

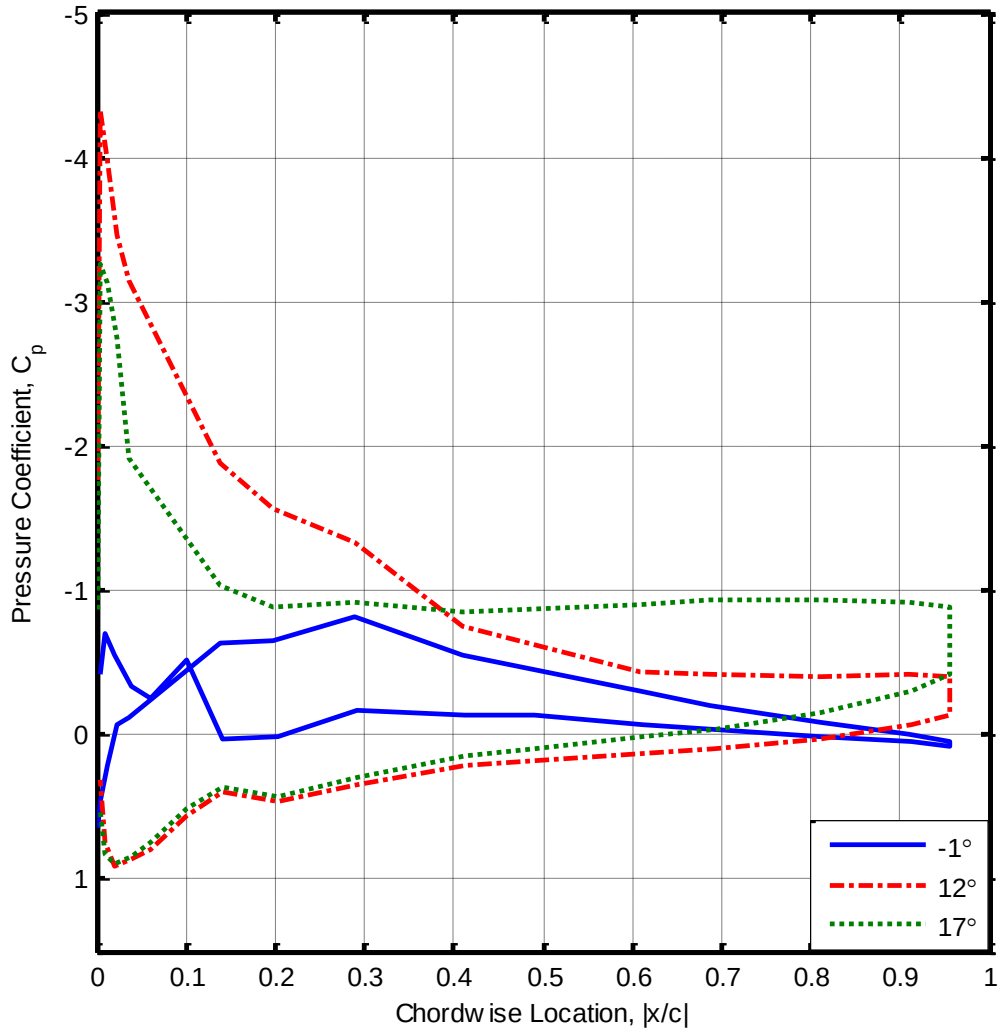

Fig. 16. C_p Distribution at a Reynolds Number of 1,000,000

From the coefficient of pressure distribution, the coefficient of lift and drag were computed. Shown in Fig. 17 is the coefficient of lift curves. At the lowest Reynolds number, the airfoil stalls at an angle of 14°. As the Reynolds number increases, the stall angle increases due to the increasingly turbulent boundary layer, which is expected. At a Reynolds number of 1,000,000, there is not as sharp of a drop in the coefficient of lift at

the stall angle, compared to the two lower Reynolds numbers. However, the magnitude of the coefficient of lift at a Reynolds number of 1,000,000 is similar to the magnitude of the coefficient of lift at a Reynolds number of 500,000, suggesting that the coefficient of pressure around the airfoil is saturated. This is also reflected in the coefficient of pressure curves, particularly at angles of -1° and 17°at these Reynolds numbers (Fig. 15 and Fig. 16). At higher angles, the flow remains attached and thus the coefficient of lift is higher at a Reynolds number of 1,000,000 when compared to a Reynolds number of 500,000.

Fig. 18 compares the coefficient of lift between the XFLR5 results and the experimental results at a Reynolds number of 500,000. The experimental results compare favorably to XFLR5. In both cases, the maximum coefficient of lift angle of attack is 15°. After an angle of attack of 15°, the behavior of the curves deviate from one another. The experimental results indicate sharp stall behavior unlike the XFLR5 results. This may be attributed to limitations of the numerical solver.

The coefficient of drag curves are shown in Fig. 19. As expected, the coefficient of drag increases with the angle of attack. At the stall angle, there is a significant increase in the coefficient of drag, due to flow separation.

Fig. 20 indicates the day-to-day repeatability of the static pressure data. As indicated, the magnitudes and trends of the curves are extremely similar. At a Reynolds number of 500,000, it seems that the stall angle varies by 1°. This is attributed to the coarse data resolution, which was limited due to time constraints.

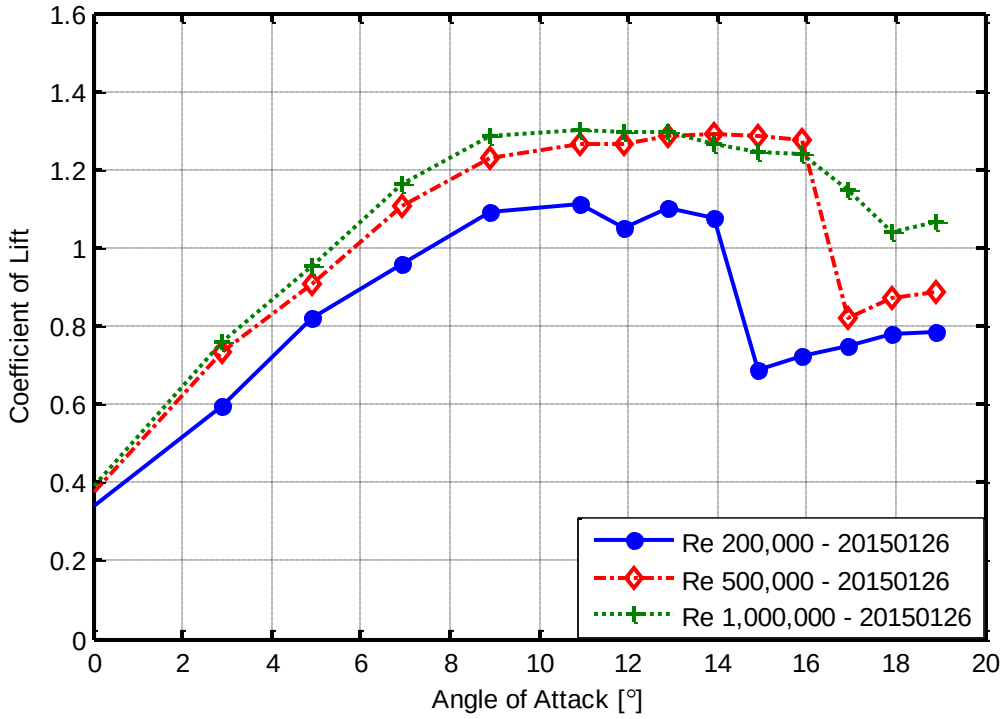

Fig. 17. Experimental C_L Curves

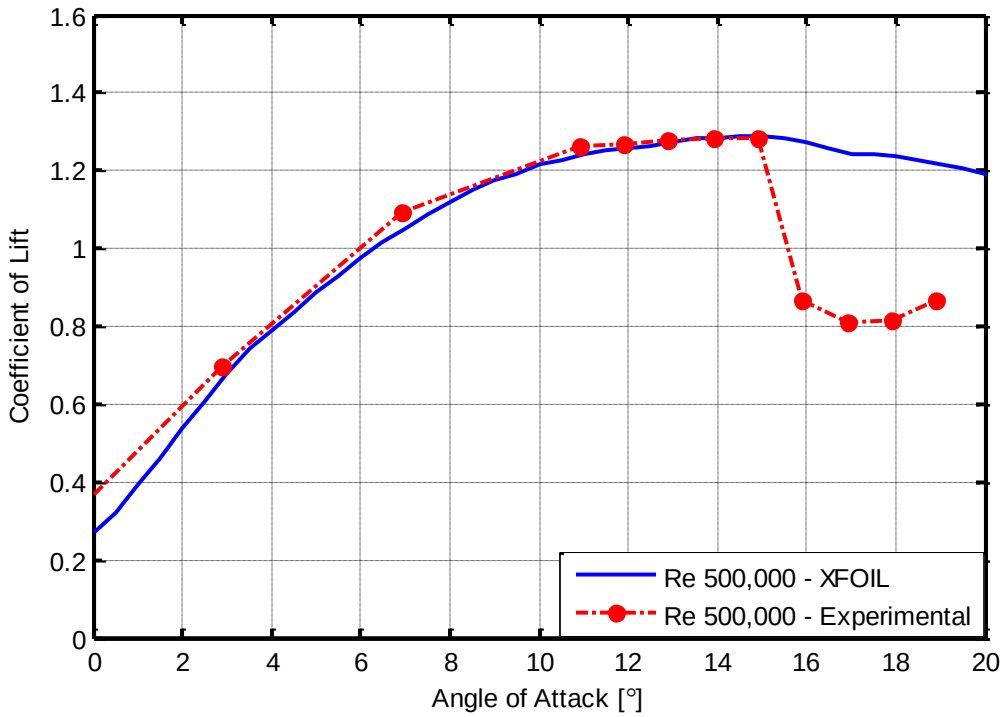

Fig. 18. Predicted Vs. Experiment C_L

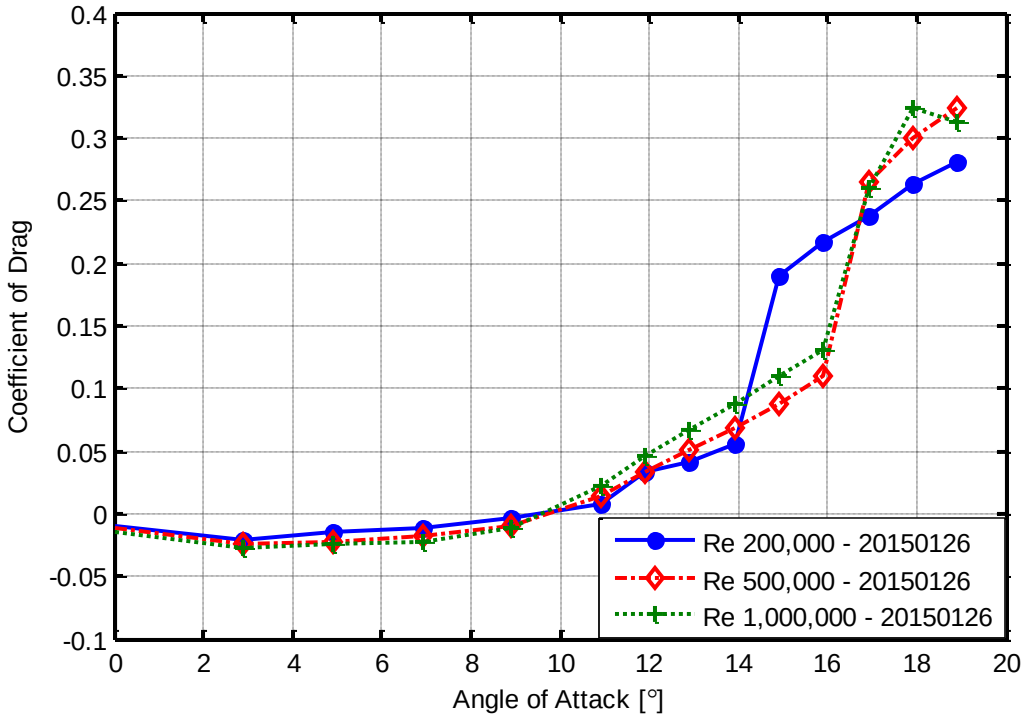

Fig. 19. Experimental C_D Curves

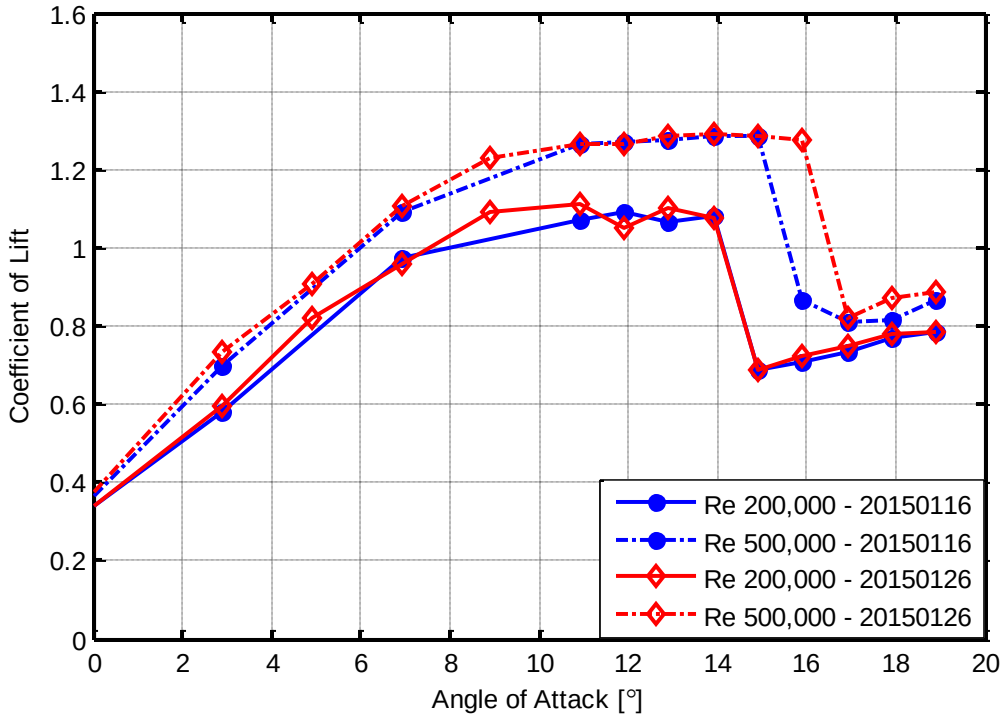

Fig. 20. Static Pressure Repeatability

B. Baseline Data – Pressure Spectra and PIV Results

From surface pressure data, it was determined that the coefficient of lift at 17° and a Reynolds number of 500,000 was 0.80 and the coefficient of drag was 0.28. A baseline coefficient of pressure curve is provided as Fig. 21. As indicated in the figure, the flow is fully separated and the stagnation point is located slightly downstream of the leading edge on the pressure side.

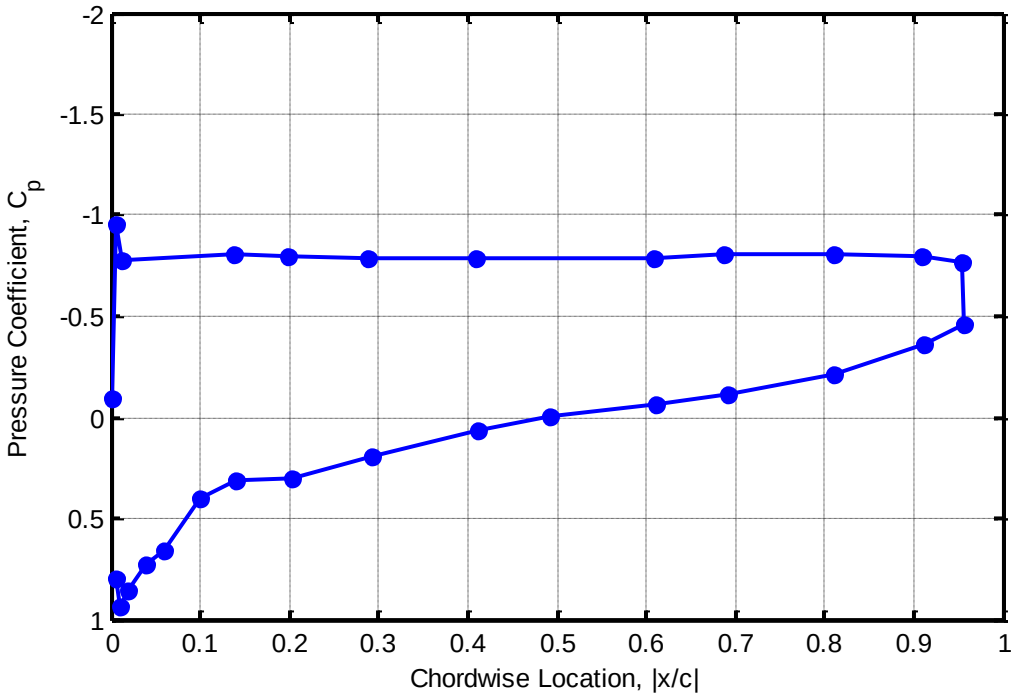

Fig. 21. Coefficient of Pressure Profile at Reynolds number of 500,000

Pressure fluctuations were measured using a microphone located outside of the shear layer of the airfoil. The baseline pressure power spectral density curve is shown in Fig. 22. This plot indicates that the Strouhal number of the dominant flow instability, the shedding of large-scale vortices, was 0.60. The first harmonic is also distinguishable and occurs at a Strouhal number of 1.20.

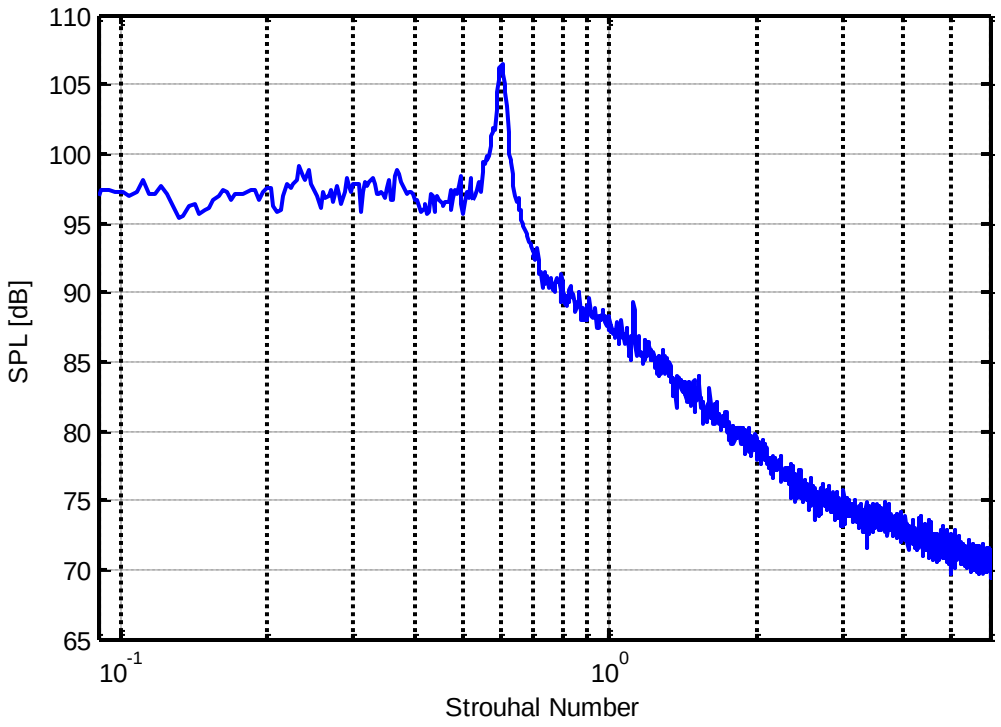

Fig. 22. Baseline Pressure Spectrum at Reynolds number of 500,000

Particle image velocimetry was also acquired to attain a visual understanding of the flow and is shown in Fig. 23. The velocity field has been normalized by the freestream velocity, u_∞. Data on the pressure side of the airfoil cannot be acquired due to the presence of the airfoil. The white line over and in the wake of the airfoil indicates the zero velocity iso-contour, which identifies the approximate separated zone. As indicated, the flow separates near the leading edge, and is consistent with the separation location found using oil-flow visualization shown in Fig. 7.

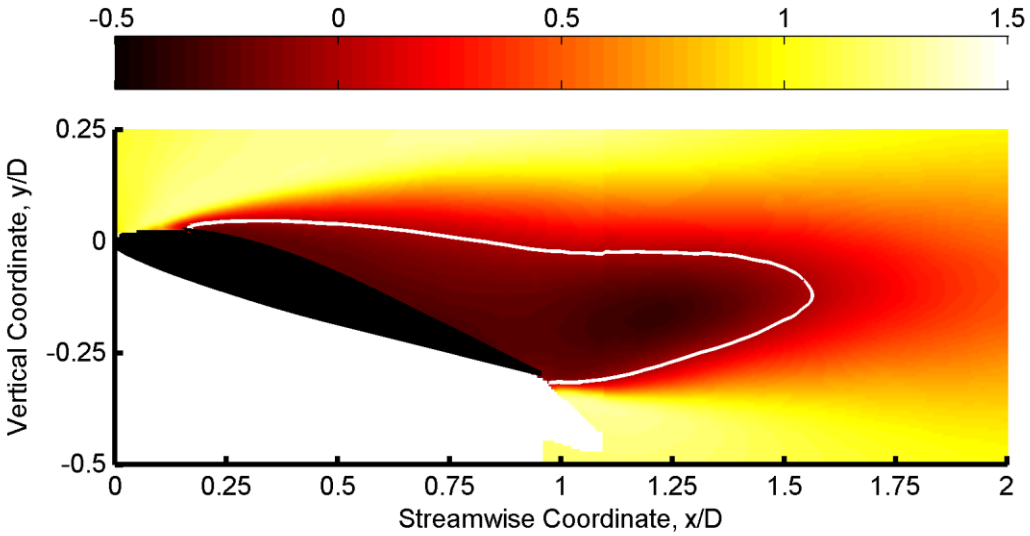

Fig. 23. Baseline PIV Data at Reynolds number of 500,000

IV. Excitation Results

Data was acquired at a Reynolds number of 500,000 and an angle of attack of 17°. The excitation Strouhal numbers included the natural shedding Strouhal number and its harmonics.

A. Surface Pressure Distribution

Surface pressure data was obtained from 28 uncovered pressure taps (5 pressure taps were covered due to the presence of the actuator) for excited cases. As shown in Fig. 15, the Boeing Vertol VR7 airfoil has a sharp pressure peak at the leading edge of the airfoil. The loss of the pressure taps near the leading edge affects the accuracy of the lift predicted. With the loss of these pressure taps, the coefficient of lift and coefficient of drag were 0.28 and 0.80 for a Strouhal number of 0 (no excitation), which are similar to the baseline values of 0.28 and 0.80. Given that the flow is fully separated, the loss of pressure taps is of little consequence in the baseline case, and thus the similarity in values is expected. However in excited cases, the coefficient of lift would be underestimated.

The coefficient of pressure distribution is shown in Fig. 24 for a baseline case and two excitation Strouhal numbers. For a Strouhal number of 0.60, which is coincident with the natural shedding Strouhal number, the coefficient of pressure on the suction side has decreased significantly, which suggests that the flow has been accelerated when compared to the baseline case. However, the coefficient of pressure is nearly constant over the suction side and thus remains detached. At higher excitation Strouhal numbers, the flow seems to be attached near the leading edge, but separates afterward.

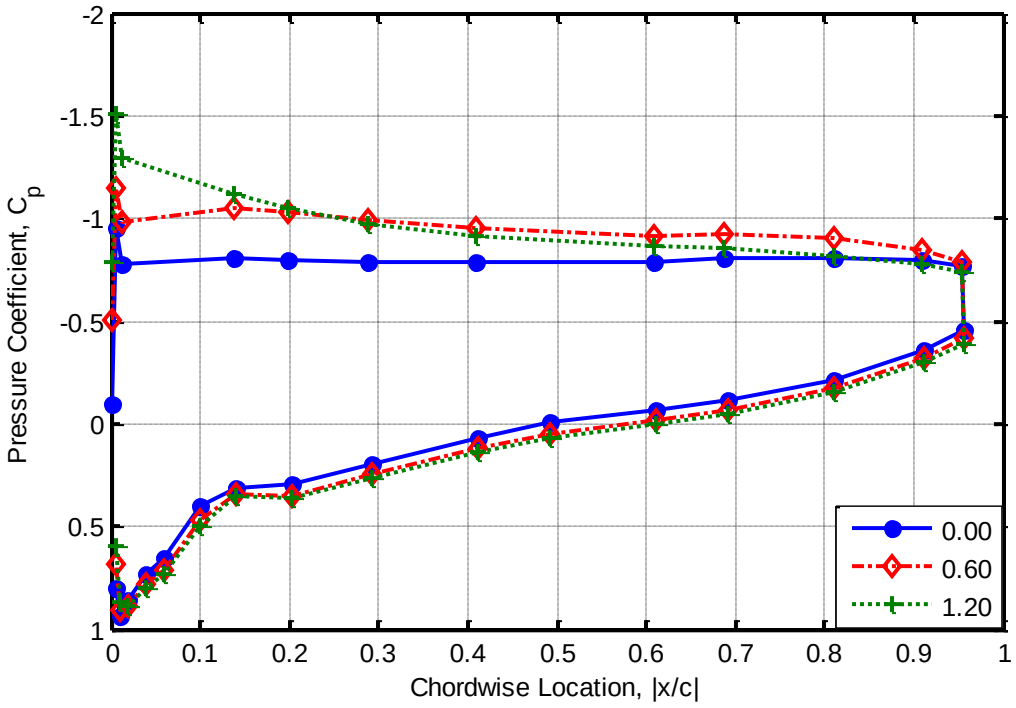

Fig. 24. Coefficient of Pressure Profiles for Excited Cases

The coefficient of lift curve (Fig. 25) indicates a similar trend (the bars shown in the figure represent the 95% confidence interval). As the excitation Strouhal number increases, the coefficient of lift increases significantly until the excitation Strouhal number matches the shedding Strouhal number. Then there is a slight dip in the coefficient of lift before increasing again. This may be attributed to mode competition.

The coefficient of drag curve is presented in Fig. 26 and also indicates the 95% confidence interval. The coefficient of drag increases slightly with the excitation Strouhal number and then decreases. The change in trend occurs at the shedding Strouhal number. Coupled with the coefficient of pressure profiles, these trends are expected. The increase in coefficient of drag at lower excitation Strouhal numbers are due to the acceleration of the air on the suction side, but no flow reattachment. However at the higher excitation

Strouhal numbers, the flow on the suction side accelerates and thus the coefficient of drag decreases.

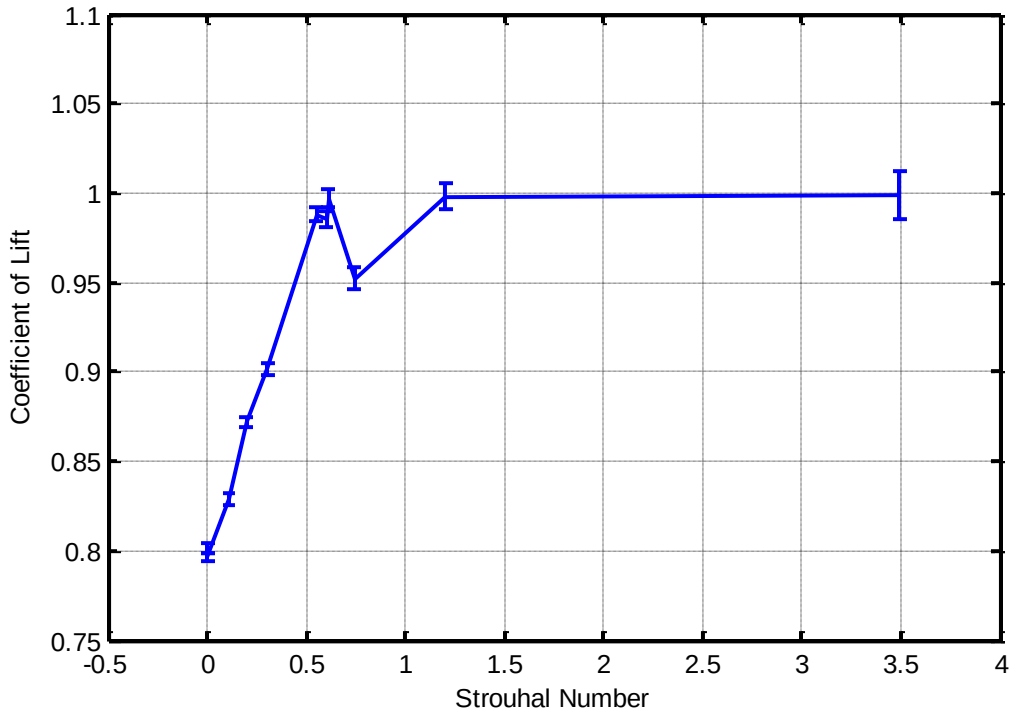

Fig. 25. Coefficient of Lift Curve for Excited Cases

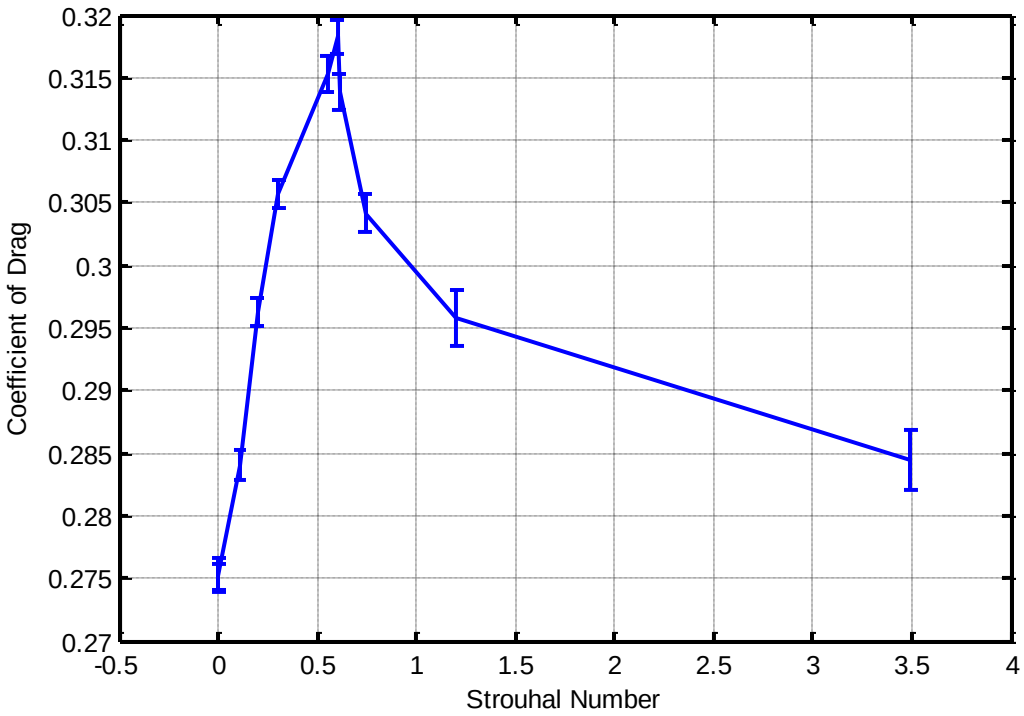

Fig. 26. Coefficient of Drag Curve for Excited Cases

An interesting observation from the coefficient of lift and drag curves is that as the excitation Strouhal number increases, so does the length of the confidence interval. For clarity, the root mean square of the coefficient of lift is plotted against the excitation Strouhal number in Fig. 27. The steady increase in the root mean square of the coefficient of lift suggests that excitation leads to the formation of span wise vortices. As these vortices convect downstream, they entrain higher momentum flow to the surface of the airfoil and increase lift momentarily. Increasing the frequency of excitation would result in a higher root mean square as these lift fluctuations become more frequent.

As such, it is expected that the root mean square of the coefficients of lift and drag would continue to increase with respects to the excitation Strouhal number.

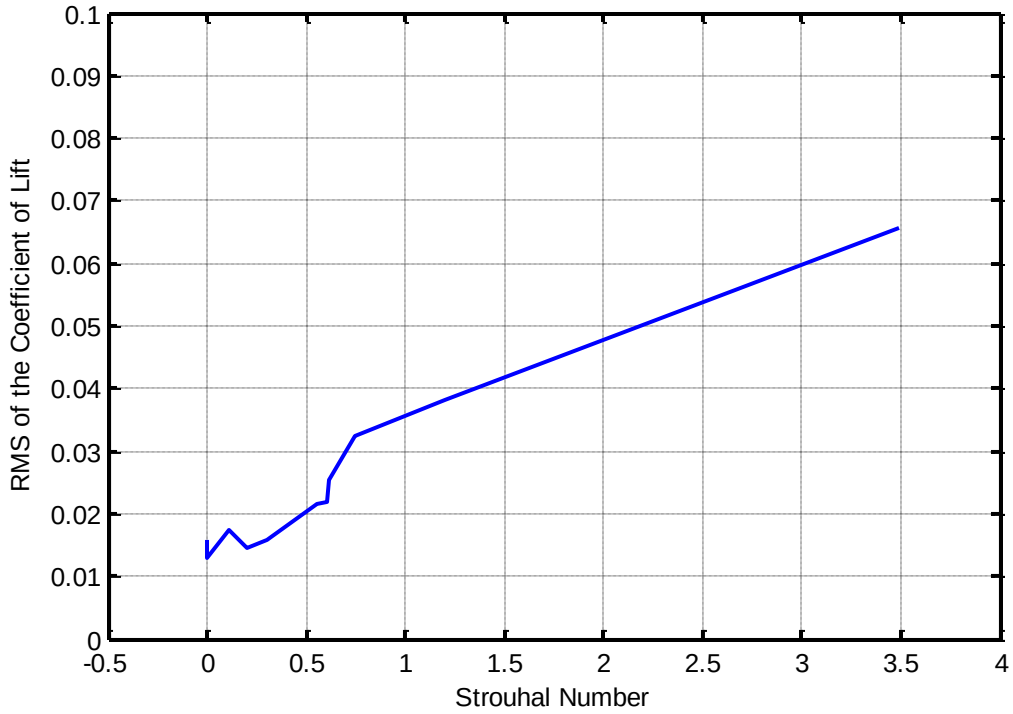

Fig. 27. RMS of the Coefficient of Lift Curve for Excited Cases

B. Fluctuating Pressure Data

Fluctuating pressure data for various excitation Strouhal numbers is presented in Fig. 28. Using a microphone at a position of $x/c = 1.75$ and $y/c = 0.4375$, fluctuating pressure data was acquired. Each curve presented in the figure, has a label on the left, which indicates the excitation Strouhal number and is separated by 20 decibels from the curve above it for clarity. This figure does not provide absolute magnitude data and thus serves for comparison of dominant features only.

For the baseline data, the natural shedding Strouhal number is 0.60. It is observed that there is a narrow peak at the excitation Strouhal number and its harmonics for nearly every case. This is consistent with the explanation outlined in the subsequent section, and

furthermore may suggest that each actuator pulse triggers the growth of a vortex which convects downstream and entrains high velocity air, increasing lift for the convective time.

At excitation Strouhal numbers near the shedding Strouhal number or its sub-harmonics ($\mathrm{St_e} = 0.20, 0.28, 0.30, 0.55, 0.60, \text{and } 0.61$), the peak at the shedding Strouhal number seems become narrow and shifts to match the excitation Strouhal number. However, unlike the rest of the excitation Strouhal numbers, it is the peak nearest to the shedding Strouhal number, which has the largest magnitude.

At higher excitation Strouhal numbers, the re-emergence of a new broadband peak is seen at a Strouhal number of 0.50. This is an interesting phenomenon, which warrants further attention; however, is not explored due to time restrictions.

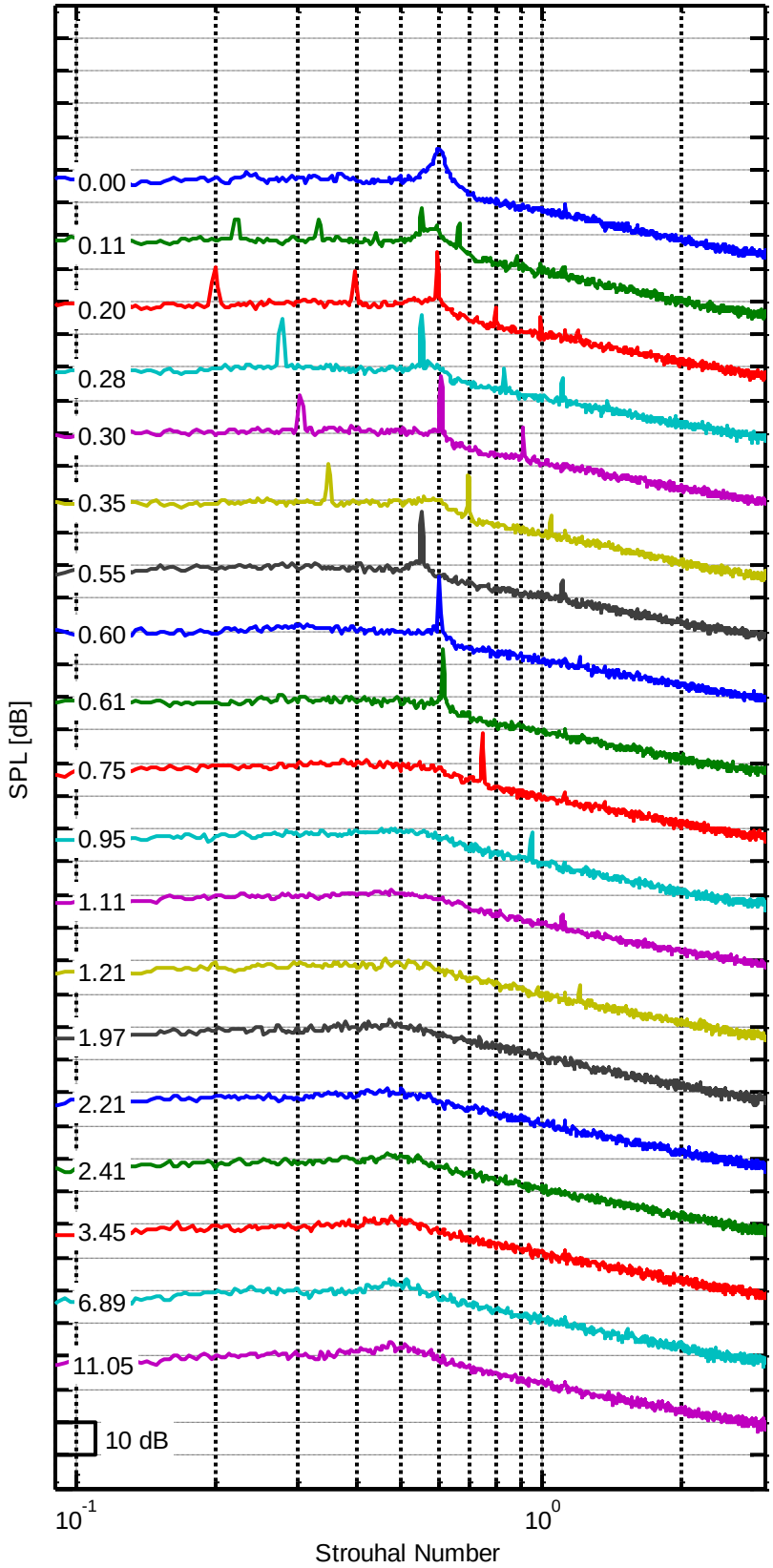

Fig. 28. Excited Acoustic Data

C. Particle Image Velocimetry

Particle image velocimetry was taken for each excitation Strouhal number presented in the surface pressure data, however only a subset is shown in this section for $\mathrm{St_e} = 0, 0.60, 1.20$ (Fig. 29, Fig. 30, and Fig. 31, respectively). In excited cases, the formation of plasma causes a bright spot at the leading edge of the airfoil, and thus is not indicative of physical flow features.

From particle image velocimetry images, it can be seen that at higher frequencies, the separation zone has been reduced and the separation started further downstream as compared to the baseline case. The separation area is plotted as a function of the excitation Strouhal number in Fig. 32.

Even when excited at relatively effective Strouhal numbers, the flow remains partially detached. This is not entirely consistent with the results found by Rethmel et al., who applied NS-DBD plasma actuators to a NACA 0015 airfoil [14]. Rethmel et al. demonstrated reattachment of the shear layer of the NACA 0015 when excited at a post stall angle of attack. This is attributed to the symmetric geometry of the NACA 0015 which consequently has less curvature than the suction side of the Boeing Vertol VR-7 airfoil. However in both cases, significant control authority is demonstrated.

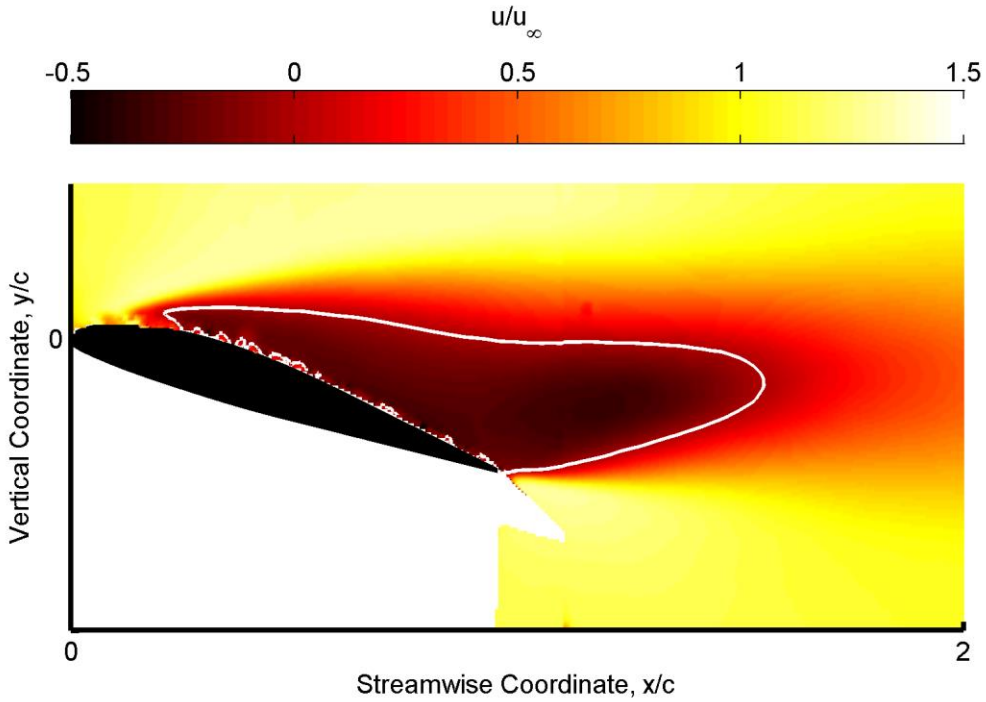

Fig. 29. Baseline ($St_e = 0$) at Reynolds number of 500,000

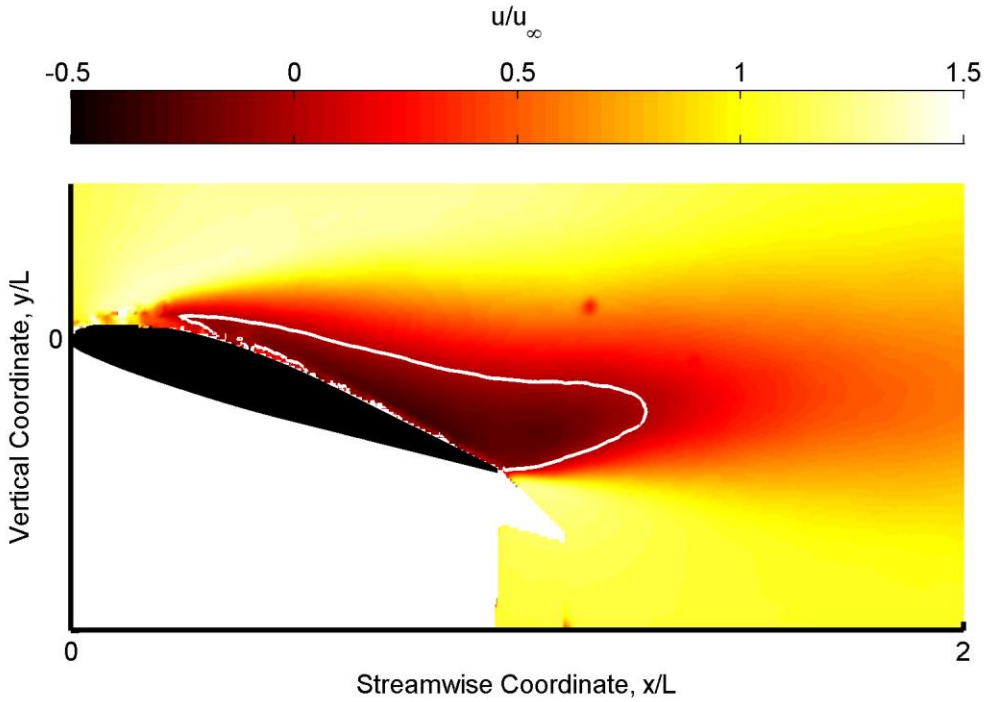

Fig. 30. $St_e = 0.60$ at Reynolds number of 500,000

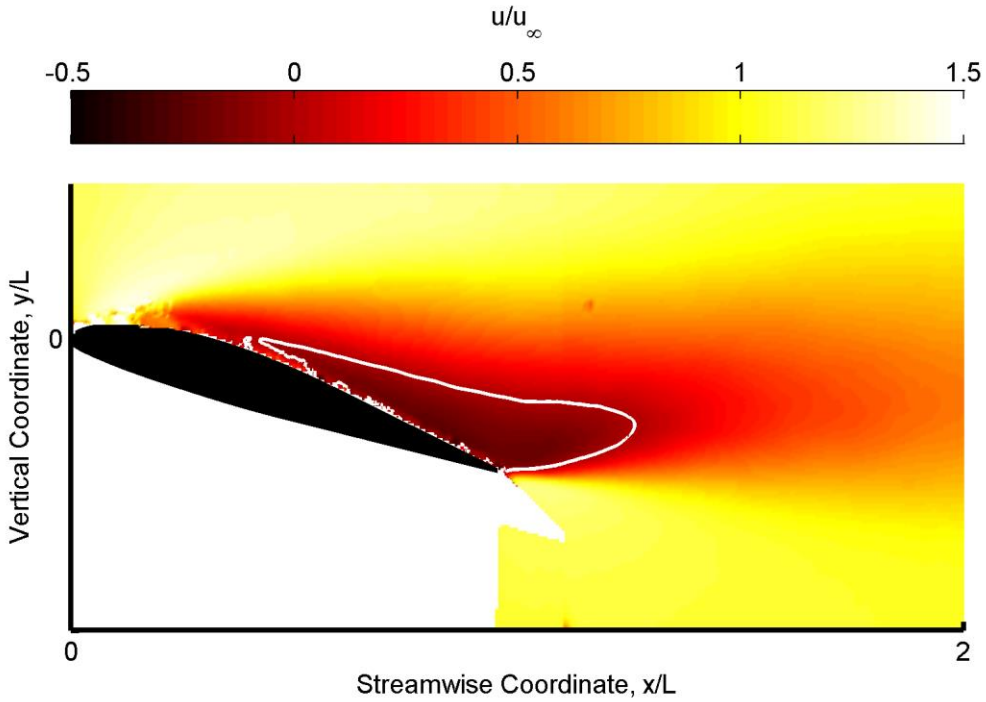

Fig. 31. $St_e = 1.20$ at Reynolds number of 500,000

Visually, at the higher excitation Strouhal numbers, the separation area is significantly smaller. The separation area is plotted in Fig. 32. As indicated in the figure, all excitation Strouhal numbers decrease the separation area. A Strouhal number of 1.20 reduces the separation area most significantly. Higher excitation Strouhal numbers do tend to decrease the separation area more so than lower ones, and the peak reduction occurs at an excitation Strouhal number of 1.20.

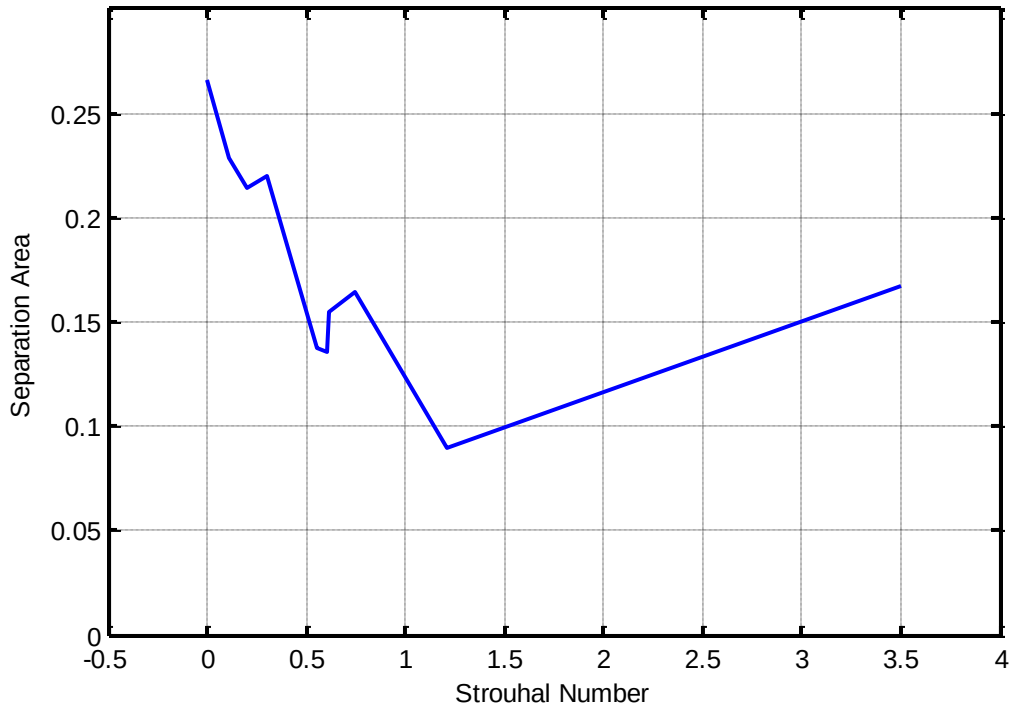

Fig. 32. Separation Area

The changes in the coefficient of lift, coefficient of drag and the separation area are shown in Fig. 33. From the figure, the coefficient of lift and separation area curves trends are mirrors of one another, as expected: in general, as the separation area decreases, the coefficient of lift increases. This holds true for all data points, except at an excitation Strouhal number of 3.45, which is the highest excited case available. This may be an anomaly, given the relatively large confidence interval of the coefficient of lift at this excitation Strouhal number that was shown in Fig. 25.

For practical application, it seems that the highest excitation Strouhal number ($St_e = 3.45$) would be optimal for control. The coefficient of lift increases by 25% for a minimal penalty in drag, which increases by 3%. At this excitation Strouhal number, the energy consumption of the actuators is 1.9 watts (in contrast, at the lowest excitation Strouhal

number tested, the energy consumption was 0.06 watts). Compared with the energy of the flow, which is 2214.6 watts, this represents an addition of 0.09% of freestream flow energy.

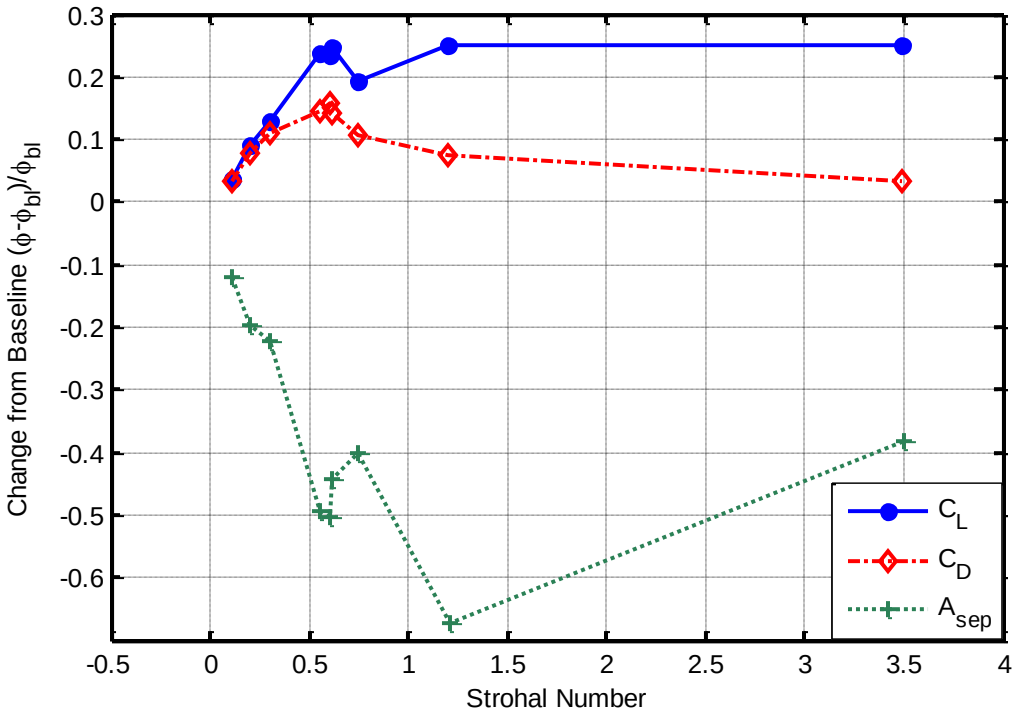

Fig. 33. Change in C_L, C_D, and A_{sep} at a Reynolds number of 500,000

Phase-locked particle image velocimetry results are shown in Fig. 34 and Fig. 35 for excitation Strouhal numbers of 0.60 and 3.45, respectively. In these figures, the swirling strength is plotted. At the moderate excitation Strouhal number, there is the formation of large, coherent structures that convect downstream. However, at higher excitation Strouhal numbers, these structures become smaller and quickly disintegrate into smaller structures. As such, this indicates the increase in the root-mean-square value with the excitation Strouhal number, as shown in Fig. 27. These results are also consistent with the fluctuating pressure data shown in Fig. 28 – at the higher excitation Strouhal numbers, the structures

do not convect downstream and thus the magnitude of the peak at this Strouhal number decreases.

At the lower and moderate excitation Strouhal number, vortex formation occurs at both the leading and trailing edge, which is unlike the higher excitation Strouhal numbers where vortex formation occurs only at the leading edge and the trailing edge behaves independently.

These images suggest that the primary mechanism of flow control is the excitation of natural flow instabilities that grow into coherent, spanwise vortices that entrain high momentum freestream flow to the surface of the airfoil, which is consistent with previous literature [14, 7].

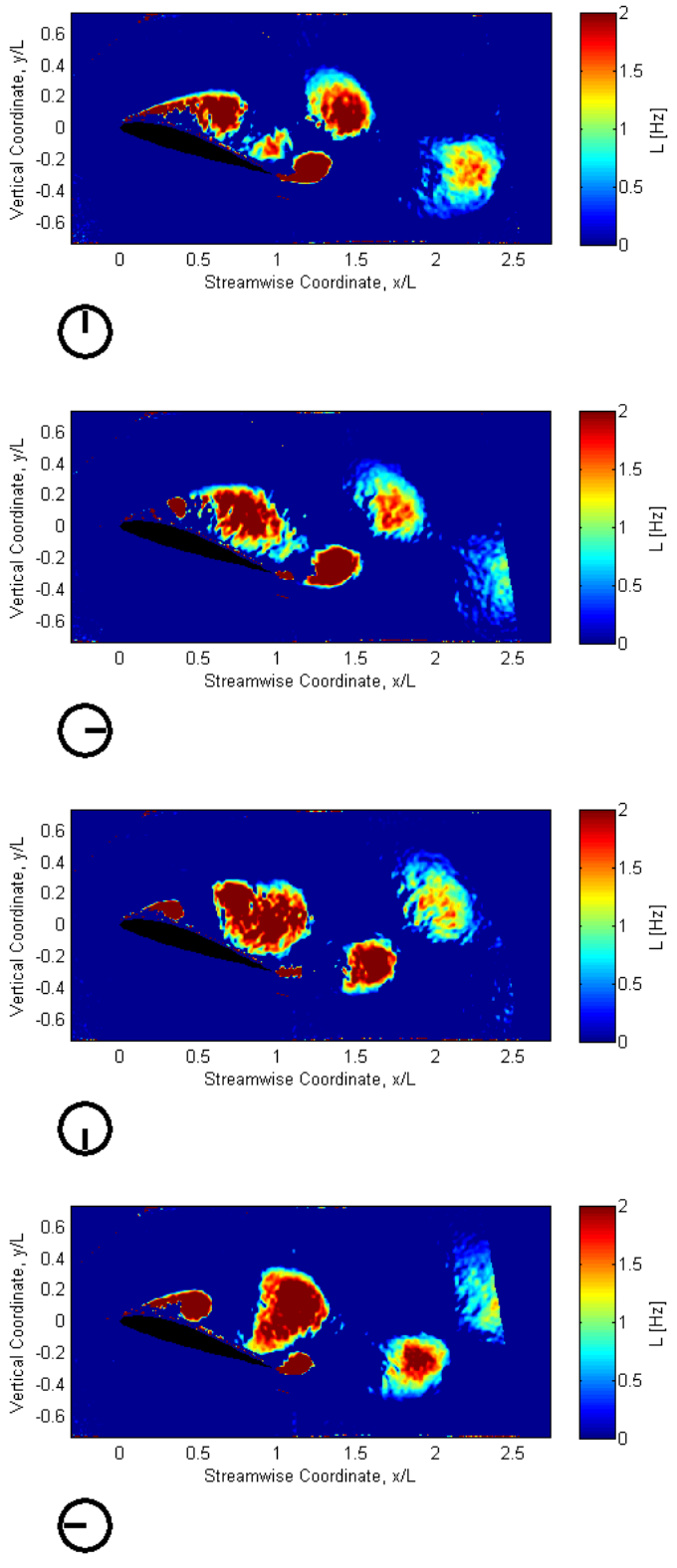

Fig. 34. Phase Locked Particle Image Velocimetry at $St_e = 0.60$

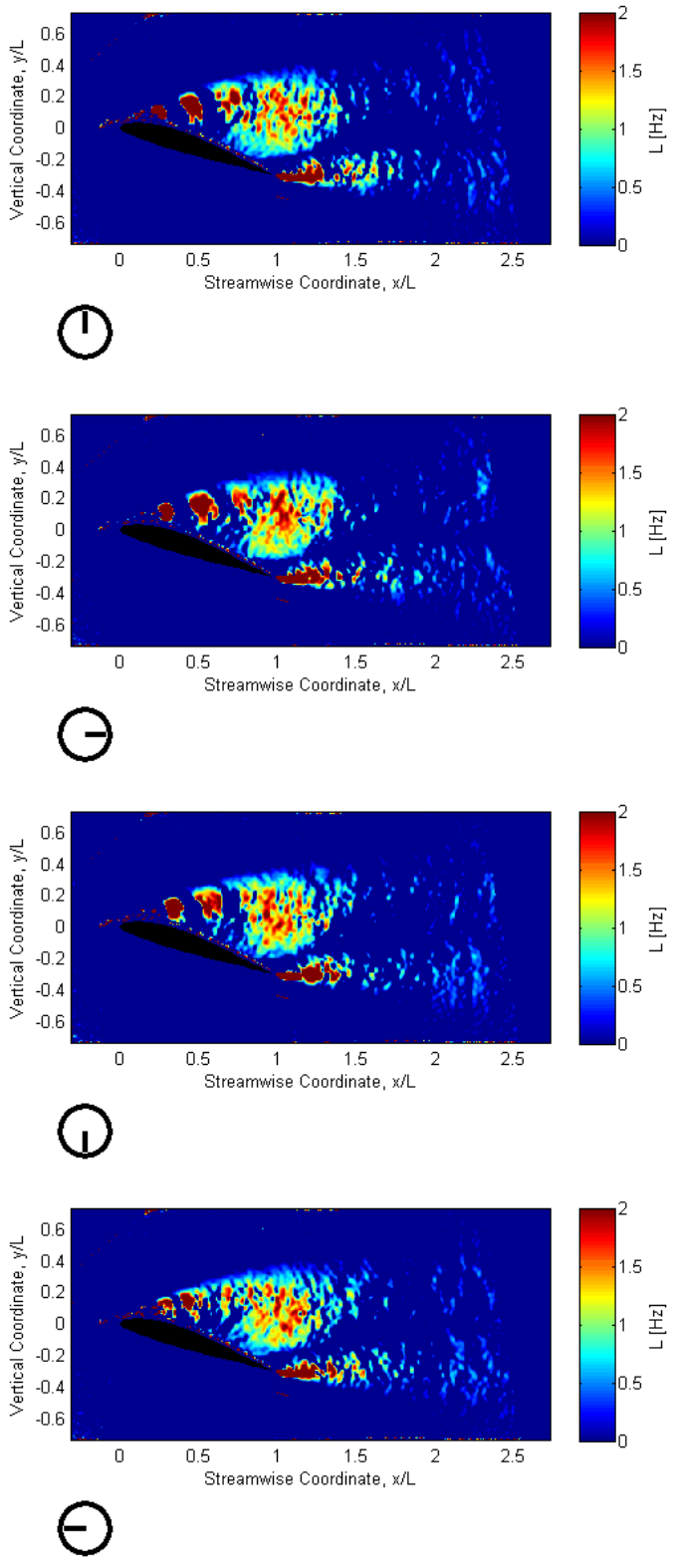

Fig. 35. Phase Locked Particle Image Velocimetry at $St_e = 3.45$

V. Conclusions

Dynamic stall is an artifact of rapidly changing angle of attack. This introduces large, unsteady loads on the airfoil, which can lead to mechanical failure of the component. In rotorcraft, dynamic pitching is unavoidable due to lift asymmetry. Thus at various phases of the rotation of the rotor, a rapid change in angle of attack is needed to ensure equal lift generation of both the advancing side and the retreating side of the rotor, potentially leading to dynamic stall.

Control of dynamic stall has been demonstrated using various blowing techniques, but remain limited at high flow velocities. As such, NS-DBD plasma actuators, which function by a thermo-acoustic mechanism, are utilized. These actuators have been shown to reattach flow at post-stall angles of attack for symmetric airfoils by perturbing natural flow instabilities, which leads to the growth of span-wise vortices that entrain freestream flow and reattach the flow.

As a precursor to dynamic stall, a Boeing Vertol VR-7 airfoil is placed at a static, post stall angle of attack in wind tunnel, where the lift and drag are characterized.

Static pressure data indicates the actuators efficacy to increase the coefficient of lift at high excitation Strouhal numbers while also increasing the coefficient of drag. At higher excitation Strouhal numbers, the coefficient of drag approaches its baseline value, unlike the coefficient of lift, which increases. It was also observed that increasing excitation Strouhal numbers, the root mean square of both the coefficient of lift and the coefficient of drag increase. This is attributed to the quickly disintegrating vortices at higher excitation Strouhal numbers.

Fluctuating pressure spectra acquired outside the shear layer of the airfoil, indicate that the excitation Strouhal number introduces a peak in the spectra at the excitation Strouhal number. Except for cases where the excitation Strouhal number is a harmonic or sub-harmonic of the shedding Strouhal number, excitation removes the shedding peak completely from the spectra. This is reflected in the phase-locked particle image velocimetry where the formation of span wise structures is tied to the excitation Strouhal number.

Particle image velocimetry indicated that the flow remained partially separated, even at higher excitation Strouhal numbers. However the velocity on the surface of the airfoil is increased, which is indicative of a higher coefficient of lift and is attributed to the entrainment of high-speed freestream fluid to the surface of the airfoil.

NS-DBD plasma actuators demonstrated control authority on the Boeing Vertol VR7 airfoil. At the optimal scenario, the coefficient of lift increases by 25% with a drag plenty of 3%. At this excitation Strouhal number, the actuators utilize 0.09% of freestream flow energy.

VI. Future Work

Phase-locked particular image velocimetry would provide a more clear understanding of the flow physics, whose effects are observed in this study. A more extensive excitation Strouhal number sweep may help explain phenomena such as the increasing root-mean-square in the coefficient of lift as well as the emergence of a peak at a Strouhal number of 0.50 in the acoustic spectrum.

In a more broad sense, understanding static stall of the airfoil at various angles of attack is needed, especially at mid-chord stall of the airfoil, before implementing the actuators in a dynamic situation.

VII. REFERENCES

[1] D. Greenblatt and I. J. Wygnanski, "The Control of Flow Separation by Periodic Excitation," Progress in Aerospace Sciences, vol. 36, no. 7, pp. 487-545, 2000.

[2] C. DuBois, "Flow Control on an Airfoil Under Reversed Flow Conditions Using Nanosecond Dielectric Barrier Discharge Actuators," MS Thesis, The Ohio State University, Columbus, 2013.

[3] D. Weaver, K. W. McAlister and J. Tso, "Control of VR-7 Dynamic Stall by Strong Steady Blowing," Journal of Aircraft, pp. 1404-1413, 2004.

[4] M. Post, "Plasma Actuators for Separation Control on Stationary and Oscillating Airfoils," PhD Thesis, University of Notre Dame, Notre Dame, 2004.

[5] H. Nagib, J. Kiedaisch, D. Greenblatt, I. Wygnanski and A. Hassan, "Effective Flow Control for Rotorcraft Applications at Flight Mach Numbers," in 31st AIAA Fluid Dynamics Conference & Exhibit, Anaheim, 2001.

[6] J. Little, K. Takashima, M. Nishihara, I. Adamovich and M. Samimy, "Separation Control with Nanosecond-Pulse-Driven Dielectric Barrier Discharge Plasma Actuators," AIAA Journal, vol. 50, no. 2, pp. 350-365, 2012.

[7] C. Clifford and M. Samimy, "Flow Control on an Airfoil in Fully-Reversed Condition with Actuation on Both Leading and Trailing Edges," in AIAA, Kissimmee, 2015.

[8] P. Martin, J. Wilson, J. B. T. Wong, M. Moulton and M. and McVeigh, "Passive Control of Compressible Dynamic Stall," AIAA, 2008.

[9] A. Seifert, A. Darabi and I. Wygnanski, "Delay of Airfoil Stall by Periodic Excitation," Journal of Aircraft, vol. 33, no. 4, pp. 691-698, 1996

[10] N. J. Bisek, J. Poggie, M. Nishihara and I. Adamovich, "Hypersonic Flow over a Cylinder with a Nanosecond Pulse Electrical Discharge," Journal of Thermophysics and Heat Transfer, vol. 28, no. 1, pp. 18-26, 2014.

[11] D. V. Roupassov, A. A. Nikipelov, M. M. Nudnova and A. Y. Starikovskii, "Flow Separation Control by Plasma Actuator with Nanosecond Pulsed-Periodic," AIAA Journal, vol. 47, no. 1, pp. 168-185, 2009.

[12] K. Takashima, Y. Zuzeek, W. R. Lempert and I. V. Adamovich, "Characterization of a Surface Dielectric Barrier Discharge Plasma Sustained by Repetitive Nanosecond Pulses," Plasma Sources Science and Technology, vol. 20, pp. 1-10, 2011.

[13] J. Little, K. Takashima, M. Nishihara, I. Adamovich and M. Samimy, "High Lift Airfoil Leading Edge Separation Control with Nanosecond Pulse Driven DBD Plasma Actuators," in 5th AIAA Flow Control Conferency, Chicago, 2010.

[14] C. Rethmel, J. Little, K. Takashima, A. Sinha, I. Adamovich and M. Samimy, "Flow Separation Control over an Airfoil with Nanosecond Pulse Driven DBD," in AIAA Aerospace Sciences Meeting, Orlando, 2011.

[15] C. Clifford, A. Singhal and M. Samimy, "Leading Edge Separation Control on an Airfoil in Fully-Reversed Conition," in AIAA Applied Aerodyanmics Conference, Alanta, 2014. (Conference Paper)

[16] K. Duraisamy, W. J. McCroskey and J. D. Baeder, "Analysis of Wind Tunnel Interference Effects on Subsonic Unsteady Airfoil Flows," Journal of Aircraft, vol. 44, no. 5, pp. 1683-1690, 2007. (Peer Reviewed Journal Article)

[17] W. J. McCroskey, K. W. McAlister, L. W. Carr and S. L. Pucci, "An Experimental Study of Dynamic Stall on Advanced Airfoil Sections Volume 1. Summary of the Experiment," NASA, Moffett Field, 1982. (Technical Report)

[18] N. D. Ligget, "Numerical Investigation of Static and Dynamic Stall of Single and Flapped Airfoils," Georgia Institute of Technology, Atlanta, 2012. (Conference Paper)

[19] K. W. McAlister and C. Tung, "Suppression of Dynamic Stall with a Leading-Edge Slat on a VR-7 Airfoil," NASA, Moffett Field, 1993. (Technical Report)

[20] K. W. McAlister, O. Lambert and D. Petot, "Application of the ONERA Model of Dynamic Stall," NASA, Moffett Field , 1984. (Technical Report)

[21] D. Weaver, K. W. McAlister and J. Tso, "Control of VR-7 Dynamic Stall by Strong Steady Blowing," Journal of Aircraft, vol. 41, no. 6, pp. 1404-1413, 2004. (Peer Reviewed Journal Article)

[22] P. Martin, J. Wilson, J. B. T. Wong, M. Moulton and M. McVeigh, "Passive Control of Compressible Dynamic Stall," in AIAA Applied Aerodynamics Conference, Honolulu, 2008. (Conference Paper)

[23] H. Nagib, J. Kiedaisch, D. Greenblatt, I. Wygnanski and A. Hassan, "Effective Flow Control for Rotorcraft Applications at Flight Mach Numbers," in AIAA Fluid Dynamics Conference and Exhibit, Anaheim, 2001.